Theory of zero-field superconducting diode effect in twisted trilayer graphene

Harley D. Scammell,[1] J.I.A. Li,[2] and Mathias S. Scheurer[3]

[1]*School of Physics, the University of New South Wales, Sydney, NSW, 2052, Australia*
[2]*Department of Physics, Brown University, Providence, RI 02912, USA*
[3]*Institute for Theoretical Physics, University of Innsbruck, Innsbruck A-6020, Austria*

In a recent experiment [Lin *et al.*, arXiv:2112.07841], the superconducting phase hosted by a heterostructure of mirror-symmetric twisted trilayer graphene and WSe₂ was shown to exhibit significantly different critical currents in opposite directions in the absence of external magnetic fields. We here develop a microscopic theory and analyze necessary conditions for this zero-field superconducting diode effect. Taking into account the spin-orbit coupling induced in trilayer graphene via the proximity effect, we classify the pairing instabilities and normal-state orders and derive which combinations are consistent with the observed diode effect, in particular, its field trainability. We perform explicit calculations of the diode effect in several different models, including the full continuum model for the system, and illuminate the relation between the diode effect and finite-momentum pairing. Our theory also provides a natural explanation of the observed sign change of the current asymmetry with doping, which can be related to an approximate chiral symmetry of the system, and of the enhanced transverse resistance above the superconducting transition. Our findings not only elucidate the rich physics of trilayer graphene on WSe₂, but also establish a means to distinguish between various candidate interaction-induced orders in spin-orbit-coupled graphene moiré systems, and could therefore serve as a guide for future experiments as well.

CONTENTS

I. INTRODUCTION

Semiconductor diodes play an essential role in modern electronics—computation, communication and sensing [1]. The diode generates a nonreciprocity, hosting low resistance in one direction, and high resistance in the opposite. In a superconducting diode, the critical supercurrent in one direction is larger than in the opposite. This feature has elicited fundamental theoretical and experimental studies to uncover the underlying mechanisms. To this end, recent reports of the superconducting diode effect—induced by magnetic field [2–8], magnetic proximity [8, 9], or magnetic Josephson or tunnel junctions [10–19]—have emerged and attracted considerable attention. Having nonreciprocity in common with the semiconductor, yet boasting zero resistance, superconducting diodes have potential as building blocks for future quantum electronics.

A recent study [20] (companion to this work) considers a heterostructure consisting of twisted trilayer graphene (tTLG) [21–26] and WSe₂, as depicted in Fig. 1, and demonstrates a superconducting diode effect in the ab-
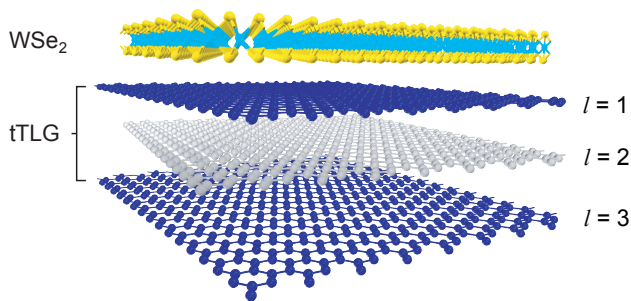
FIG. 1: Schematic of the tTLG and WSe$_2$ heterostrucure; graphene layers are labelled by $l = 1, 2, 3$, and have alternating twist angles such that the tTLG subsystem is mirror symmetric.

sence of external magnetic fields, magnetic proximity or a magnetic junction; for brevity, we here refer to this effect as the zero-field superconducting diode effect (ZFDE). In addition, several revealing features of the ZFDE were reported: (i) the diode effect, i.e., the asymmetry δJ_c of the current along opposite directions, can be trained by a small out-of-plane magnetic field, (ii) δJ_c can be reversed by doping, and (iii) the system exhibits an enhanced transverse resistance in a small temperature range above the superconducting T_c. "Untraining" the ZFDE, also suppresses this enhancement, implying a direct connection to the diode effect.

The emergence of a ZFDE in tTLG/WSe$_2$ implies a co-existence between superconductivity and spontaneously broken time-reversal and C_{2z} symmetries. Such a co-existence is a rare occurrence—superconducting states are typically restricted to systems whereby pairing occurs between time-reversed partners. Establishing an understanding of the ZFDE is therefore of fundamental concern. Moreover, understanding the manipulation of the ZFDE—as per the observations (i–iii)—offers potential for future technological applications. The reported phenomenology of superconductivity and possible related instabilities in tTLG on WSe$_2$ [20] therefore offers an exciting challenge to theory, and demands examination.

The purpose of this work is to provide a theoretical understanding of the phenomenology of the tTLG/WSe$_2$ heterostructure, with a primary focus on the ZFDE. Our analysis comprises general symmetry arguments as well as explicit model calculations, which taken together illuminate the ZFDE, the possible superconducting and normal-state instabilities of the system, the emergence of vestigial orders, and the influence of spin-orbit coupling (SOC) and external magnetic fields. It also provides important constraints on the possible origins of the ZFDE in [20] which, in turn, reveal information about the many-body physics in the tTLG/WSe$_2$ heterostructure. Moreover, our analysis offers an explanation of the findings (i–iii). In particular, we consider a

diode effect arising due to coexistence of superconductivity and a normal-state order, and determine the symmetry requirements—namely, which perturbation (or combination) out of SOC, strain and displacement field are sufficient—for the ZFDE and the its field training [see (i) above]. We find that only a small set of (four) possible normal state orders are consistent with the observed field trainabiltiy, and which further become symmetry equivalent in the limit of strong SOC. We provide an explanation of the doping dependence (ii) of the diode effect, which can be understood by invoking the approximate chiral symmetry of the moiré bands. And, concerning (iii), we argue how vestigial nematic order arises, and that quite generally it is expected to remain ordered above, yet in the vicinity of, the superconducting critical temperature—in which case offering an explanation of the enhanced transverse resistance reported [20]. Additionally, we show that there is one unconventional pairing state that spontaneously breaks time-reversal symmetry and allows for a ZFDE without normal-state order. Along the way, we illuminate the relation between finite-momentum pairing and the diode effect.

The rest of the paper is organized as follows: We begin in Sec. II by providing a continuum noninteracting model of the tTLG setup, and present the symmetries on the model. In Sec. III we discuss the possible pairing states in tTLG starting from zero SOC, and adiabatically turning it on. In Sec. IV we provide a detailed symmetry analysis of the diode effect: determining which candidate normal-state orders can support the ZDE; finding which orders allow for magnetic field training of the diode effect; and finally presenting a means to generate the ZDE without normal state order. In Sec. V we turn to explicit model calculations, presenting first the general formalism to compute the critical current, and subsequently applying it to a semi-analytic patch theory, toy models on the full MBZ, and finally to the full continuum model of tTLG with and without SOC. In Sec. VI we turn to a curious and striking experimental feature—the doping dependence of the diode effect—and present a mechanism that explains the experimental observations thereof [20]. Conclusion and outlook are provided in Sec. VII

II. MODEL AND SYMMETRIES

To set the stage for the analysis in the subsequent section, we will here define the models we will use for tTLG on WSe$_2$ throughout this work, and discuss its symmetries.

A. Notation and continuum model

The heterostructure studied in Ref. 20 consists of tTLG near its magic angle and WSe$_2$, as depicted in

Fig. 1. To describe the three layers, $l = 1, 2, 3$, of graphene with alternating twist angle, we will employ the three-layer generalization of the commonly used continuum model of twisted-bilayer graphene [27–29], where the magic angle occurs at around $1.58°$. The impact of WSe$_2$ is taken into account via the proximity-induced spin-orbit terms [30, 31]. Starting in a real-space description, with $c^\dagger_{\boldsymbol{r};\rho,l,\eta,s}$ denoting the creating operator of an electron at position $\boldsymbol{r} \in \mathbb{R}^2$, on sublattice ρ, in layer l, valley η, and of spin s, the non-interacting Hamiltonian can be written as

$$H_0 = \int \mathrm{d}\boldsymbol{r}\, c^\dagger_{\boldsymbol{r}}\, h(\boldsymbol{r}, \boldsymbol{\nabla})\, c_{\boldsymbol{r}}, \qquad (2.1\mathrm{a})$$

where h is a matrix in sublattice, layer, valley, and spin space [indices suppressed in Eq. (2.1a)] and consists of the following terms

$$h = \sum_{l=1}^{3} h^{\mathrm{g}}_l + h^{\mathrm{t}} + h^{\mathrm{D}} + h^{\mathrm{SOC}}. \qquad (2.1\mathrm{b})$$

Here, h^{g}_l, $l = 1, 2, 3$, are the Dirac Hamiltonians associated with each individual graphene layer l, twisted by angle $\theta_l = (-1)^l \theta/2$; it reads as $h^{\mathrm{g}}_l = -iv_F e^{i\frac{\theta_l}{2}\rho_3} \boldsymbol{\rho}_\eta \boldsymbol{\nabla} e^{-i\frac{\theta_l}{2}\rho_3}$, where $\boldsymbol{\rho}_\eta = (\eta_z \rho_x, \rho_y)$ and ρ_j are Pauli matrices in sublattice space. The second term in Eq. (2.1b) captures the tunneling between adjacent graphene layers, $(h^{\mathrm{t}})_{\rho,l,\eta,s;\rho',l',\eta',s'} = \delta_{s,s'}\delta_{\eta,\eta'}(\delta_{l+1,l'}T_{\eta\boldsymbol{r}} + \mathrm{H.c.})_{\rho,\rho'}$, which is modulated on the moiré scale [28], $T_{+,\boldsymbol{r}} = e^{-i\boldsymbol{q}_1\boldsymbol{r}}[\mathcal{T}_1 + \mathcal{T}_2 e^{-i\boldsymbol{G}_1\boldsymbol{r}} + \mathcal{T}_3 e^{-i(\boldsymbol{G}_1+\boldsymbol{G}_2)\boldsymbol{r}}] = T^*_{-,\boldsymbol{r}}$. The momenta involved here are the momentum transfer, $\boldsymbol{q}_1 = k_\theta(0,-1)$, $k_\theta = 2|\mathrm{K}_g|\sin(\theta/2)$, from the K to the K$'$ point at the corners of the moiré Brillouin zone (MBZ) as well as the basis vectors, $\boldsymbol{G}_1 = -\sqrt{3}k_\theta(1,\sqrt{3})^T/2$ and $\boldsymbol{G}_2 = \sqrt{3}k_\theta(1,0)^T$, of the reciprocal moiré lattice (RML). In this expression, $\mathcal{T}_j$ are matrices in sublattice space which only exhibit two independent real parameters—the intra (w_0) and intersublattice (w_1) hopping—and can be written as $\mathcal{T}_j = [w_0\rho_0 + w_1 e^{i\frac{2\pi}{3}(1-j)}(\rho_x + i\rho_y) + \mathrm{H.c.}]/2$. Since h^{t} breaks the continuous translation symmetry of the Dirac Hamiltonians h^{g}_l but preserves translations on the moiré scale, it reconstructs the Dirac cones into moiré bands. The latter are derived by Fourier transformation of $c_{\boldsymbol{r};\rho,l,\eta,s}$, leading to the momentum-space operators $c_{\boldsymbol{k};\rho,l,\eta,s,\boldsymbol{G}}$ where $\boldsymbol{k} \in$ MBZ and $\boldsymbol{G} \in$ RML. For convenience, Appendix A provides the explicit form of the continuum model Eq. (2.1) written in momentum space.

The third term in Eq. (2.1b) describes the impact of a perpendicular electric field (displacement field) D_0 and is given by $(h^{\mathrm{D}})_{l,l'} = D_0\rho_0\eta_0 s_0\delta_{l,l'}(\delta_{l,1} - \delta_{l,3})$, where we use, as above, the same symbol for Pauli matrices and the associated index, i.e., ρ_j, η_j, and s_j are Pauli matrices in sublattice, valley, and spin space, respectively.

Finally, the last term in Eq. (2.1b) captures the impact of the WSe$_2$ crystal and, thus, constitutes the cru-

cial difference between tTLG and the system that has been shown to exhibit a diode effect in Ref. 20. It is also the part of the Hamiltonian (2.1b) that has not been discussed in previous theoretical works on tTLG [32–34]. The form of h^{SOC} we use is motivated by the fact that the overlap of wavefunctions of WSe$_2$ and of the graphene layers $l = 2, 3$ in Fig. 1 is negligibly small and, hence, the proximity effect predominately affects the graphene layer $l = 1$ and, in that layer, is of the same form as for a single layer of graphene on WSe$_2$. Furthermore, to capture the relevant low-energy moiré bands it is sufficient to use the single-layer model expanded around each Dirac cone. This is not only true for h^{g}_l but also for the impact of SOC. So we can focus on the leading, momentum-independent, terms in h^{SOC} which can be written as [30]

$$\begin{aligned} h^{\mathrm{SOC}} = P_1 \Big[& \lambda_{\mathrm{I}} s_z \eta_z + \lambda_{\mathrm{R}} (\eta_z \rho_x s_y - \rho_y s_x) \\ & + \lambda_{\mathrm{KM}} \eta_z \rho_z s_z + m\rho_z \Big], \end{aligned} \qquad (2.2)$$

where $(P_1)_{l,l'} = \delta_{l,l'}\delta_{l,1}$ projects onto the first graphene layer. The first three contributions in Eq. (2.2) are SOC terms as they intertwine spin, $\boldsymbol{s}$, with orbital degrees of freedom, in this case valley and sublattice. These terms are often referred to as "Ising" (λ_{I}), "Rashba" (λ_{R}), and a "Kane-Mele" (λ_{KM}) SOC. The last term in Eq. (2.2) is a sublattice-imbalance term that can also be induced by the WSe$_2$.

Recent first-principle calculations [31] show that, in particular for the rather large twist angles between WSe$_2$ and graphene in experiment [20], m and λ_{KM} are much smaller than λ_{I} and λ_{R}. While our analysis can be straightforwardly generalized to include both m and λ_{KM}, we set $m = \lambda_{\mathrm{KM}} = 0$ from here on, to simplify the presentation of the results. Additionally, we note that to partially account for relaxation effects, we take $w_0/w_1 = 0.875$, with $w_1 = 110$ meV, these values are chosen to best agree with experiment [35]. Finally, for demonstration in Section V D, we will specialize to twist angle $1.5°$, which lies within the range of twist angles considered experimentally [20].

B. Symmetries

Having motivated and defined the model, H_0, we use, let us next discuss its symmetries. As the symmetries of the continuum-model description of tTLG without WSe$_2$ have already been discussed in detail in previous theoretical works [36, 37], we will here focus on the modifications when λ_{I} and/or λ_{R} in Eq. (2.2) are non-zero.

As with any SOC term, both λ_{I} and/or λ_{R} break the spin-rotation symmetry, SO(3)$_s$; while λ_{I} leaves a residual spin-rotation along the s_3 axis as a symmetry, hence, the name "Ising SOC", λ_{R} breaks SO(3)$_s$ completely. This is summarized in the first two lines of Ta-

TABLE I: Action of the different point symmetries S on the microscopic field operators ($\psi_{\boldsymbol{k}}$) of the continuum-model description of tTLG (see Sec. II A) and on the operators $f_{\boldsymbol{k}}$ in Eq. (2.3) for the Bloch states closest to the Fermi level. The last column shows which of strain, β, Rashba, λ_{R}, and Ising, λ_{I}, SOC break the respective symmetry. As in the main text, we use ρ_j, η_j, and s_j to denote Pauli matrices in sublattice, valley, and spin space. Note that Θ and Θ_s are anti-unitary operators.

S	$S\psi_{\boldsymbol{k};\ell,\boldsymbol{G}}S^\dagger$	$Sf_{\boldsymbol{k}}S^\dagger$	broken by
$\mathrm{SO(3)}_s$	$e^{i\boldsymbol{\varphi}\cdot\boldsymbol{s}}\psi_{\boldsymbol{k};\ell,\boldsymbol{G}}$	$e^{i\boldsymbol{\varphi}\cdot\boldsymbol{s}}f_{\boldsymbol{k}}$	$\lambda_{\mathrm{R}},\lambda_{\mathrm{I}}$
$\mathrm{SO(2)}_s$	$e^{i\varphi s_z}\psi_{\boldsymbol{k};\ell,\boldsymbol{G}}$	$e^{i\varphi s_z}f_{\boldsymbol{k}}$	λ_{R}
C_{3z}	$e^{i\frac{2\pi}{3}\rho_z\eta_z}\psi_{C_{3z}\boldsymbol{k};\ell,C_{3z}\boldsymbol{G}}$	$f_{C_{3z}\boldsymbol{k}}$	$\lambda_{\mathrm{R}},\beta$
C_{3z}^s	$e^{i\frac{2\pi}{3}(\rho_z\eta_z+s_z)}\psi_{C_{3z}\boldsymbol{k};\ell,C_{3z}\boldsymbol{G}}$	$e^{i\frac{2\pi}{3}s_z}f_{C_{3z}\boldsymbol{k}}$	β
C_{2z}	$\eta_x\rho_x\psi_{-\boldsymbol{k};\ell,-\boldsymbol{G}}$	$\eta_x f_{-\boldsymbol{k}}$	$\lambda_{\mathrm{R}},\lambda_{\mathrm{I}}$
C_{2z}^s	$s_z\eta_x\rho_x\psi_{-\boldsymbol{k};\ell,-\boldsymbol{G}}$	$s_z\eta_x f_{-\boldsymbol{k}}$	λ_{I}
$C_{2z}^{s'}$	$s_{x,y}\eta_x\rho_x\psi_{-\boldsymbol{k};\ell,-\boldsymbol{G}}$	$s_{x,y}\eta_x f_{-\boldsymbol{k}}$	λ_{R}
σ_h	$(1,1,-1)_\ell\psi_{\boldsymbol{k};\ell,\boldsymbol{G}}$	$\pm f_{\boldsymbol{k}}$	$D_0,\lambda_{\mathrm{R}},\lambda_{\mathrm{I}}$
I	$\eta_x\rho_x(1,1,-1)_\ell\psi_{-\boldsymbol{k};\ell,\boldsymbol{G}}$	$\pm\eta_x f_{-\boldsymbol{k}}$	$D_0,\lambda_{\mathrm{R}},\lambda_{\mathrm{I}}$
Θ	$\eta_x\psi_{-\boldsymbol{k};\ell,-\boldsymbol{G}}$	$\eta_x f_{-\boldsymbol{k}}$	$\lambda_{\mathrm{R}},\lambda_{\mathrm{I}}$
Θ^s	$is_y\eta_x\psi_{-\boldsymbol{k};\ell,-\boldsymbol{G}}$	$is_y\eta_x f_{-\boldsymbol{k}}$	—
$\mathrm{U(1)}_v$	$e^{i\varphi\eta_z}\psi_{\boldsymbol{k};\ell,\boldsymbol{G}}$	$e^{i\varphi\eta_z}f_{\boldsymbol{k}}$	—

ble I, where we also list the action of symmetries in the continuum model outlined in Sec. II A above. For simplicity and future reference, we use $\psi_{\boldsymbol{k};\rho,\ell,\eta,s,\boldsymbol{G}}$ to define the representation of the symmetries in Table I; these operators are related to $c_{\boldsymbol{k};\rho,l,\eta,s,\boldsymbol{G}}$ by a unitary transformation in layer space [38], $c_{\boldsymbol{r};\rho,l,\eta,s}=V_{l,\ell}\psi_{\boldsymbol{r};\rho,\ell,\eta,s}$, such that $\ell=1,2$ correspond to the mirror-even (invariant under σ_h which interchanges the top and bottom layers of tTLG) and $\ell=3$ to the mirror-odd (odd under σ_h) sector.

Furthermore, the SOC terms intertwine symmetries in real space with symmetries in spin space: while spin-less two-fold rotational symmetry, C_{2z}, is broken by both λ_{I} and λ_{R}, a certain combination of C_{2z} and a rotation in spin-space, which we denote by C_{2z}^s ($C_{2z}^{s'}$) in Table I, is preserved if only λ_{R} (λ_{I}) is non-zero. Note that there is no two-fold out-of-plane rotation symmetry left once both λ_{I} and λ_{R} are non-zero. Similarly, once $\lambda_{\mathrm{R}}\neq0$, spin-less C_{3z} is not a symmetry either, while a combination with a three-fold spin-rotation, C_{3z}^s, will remain a symmetry for any value of λ_{I} and λ_{R}. This symmetry is only broken if either strain is present in the samples [39–41] or if the system develops electronic nematic order [41–45]. We refer to [46] and [47] for a microscopic description of strain and nematic order in graphene moiré systems and here only use a phenomenological parameter β to describe the presence ($\beta\neq0$) or absence ($\beta=0$) of strain in our analysis. Furthermore, also spin-less time-reversal symmetry, Θ, is broken once any of the SOC terms is

non-zero, but its spin-full analogue, Θ^s, is always preserved by the non-interacting bandstructure. The same holds for $\mathrm{U(1)}_v$ symmetry, see last line in Table I: as h in Eq. (2.1b) is diagonal in the valley index, the model conserves charge in the two valleys separately.

As is clear geometrically, see Fig. 1, the mirror symmetry σ_h is not only broken by a displacement field but also by the presence of WSe$_2$ on only one side of tTLG. This is why both λ_{I} and λ_{R} [and any term in Eq. (2.2) for that matter] break σ_h, which leads to an admixture of mirror-odd and mirror-even bands. Since three-dimensional inversion symmetry, I, is simply the product of a two-fold out-of-plane rotation and σ_h, the same holds for I.

C. Effective low-energy descriptions

While we use the full continuum model in Eq. (2.1) to compute the moiré bands in the vicinity of the charge neutrality point, we focus on those bands closest to the Fermi level when studying superconductivity and the diode effect below. For a given value of the filling fraction ν, let us denote the creation operator of an electron in the band that is closest to the Fermi level at momentum $\boldsymbol{k}\in\mathrm{MBZ}$, of spin species s, and in valley η by $f_{\boldsymbol{k},\eta,s}$. Focusing only on these low-energy electronic degrees of freedom, H_0 in Eq. (2.1a) can be approximated by the effective Hamiltonian,

$$H_0^{\mathrm{LE}}=\sum_{\boldsymbol{k}\in\mathrm{MBZ}}f_{\boldsymbol{k},\eta,s}^\dagger\left(h_{\boldsymbol{k};\eta}^{\mathrm{LE}}\right)_{s,s'}f_{\boldsymbol{k},\eta,s'}, \qquad (2.3)$$

which has to be diagonal in η due to $\mathrm{U(1)}_v$ and Θ^s imposes the constraint $h_{\boldsymbol{k};\eta}^{\mathrm{LE}}=s_2(h_{-\boldsymbol{k};-\eta}^{\mathrm{LE}})s_2$. In Table I, we list the representation of the symmetries discussed in Sec. II B above, after appropriate gauge fixing. For instance and future reference, if $\lambda_{\mathrm{R}}=0$, $\mathrm{SO(2)}_s$ and Θ^s imply

$$h_{\boldsymbol{k};\eta}^{\mathrm{LE}}=\xi_{\eta\cdot\boldsymbol{k}}+\zeta_{\eta\cdot\boldsymbol{k}}\,s_z\eta, \qquad (2.4)$$

where $\xi_{\boldsymbol{k}}$ and $\zeta_{\boldsymbol{k}}$ are smooth functions of momentum [only constrained by $\xi_{\boldsymbol{k}}=\xi_{C_{3z}\boldsymbol{k}}$ and $\zeta_{\boldsymbol{k}}=\zeta_{C_{3z}\boldsymbol{k}}$ if $\beta=0$]. Note that $\zeta_{\boldsymbol{k}}$ is odd under $\lambda_{\mathrm{I}}\to-\lambda_{\mathrm{I}}$ and thus vanishes if $\lambda_{\mathrm{I}}=0$.

III. SUPERCONDUCTING ORDER PARAMETERS

We here discuss the possible pairing states in the system by starting from trilayer in the absence of WSe$_2$ and adiabatically following its pairing states, in particular, the admixture of further components to them, upon turning on the proximity-induced SOC terms λ_{I} and λ_{R} in Eq. (2.2).

For now, we will assume that the normal state, in particular, its symmetries, out of which superconductivity emerges is well described by the model in Eq. (2.1) and postpone the discussion of additional symmetry-breaking particle-hole instabilities to Sec. IV. As such, the normal state exhibits time-reversal symmetry Θ^s and it is natural to focus on pairing between electrons with opposite momenta and opposite valley quantum numbers. Using the low-energy description introduced in Sec. II C, the coupling between the superconducting order parameter $\Delta_{\boldsymbol{k};\eta}$ and the fermions can be written as

$$\Delta H_{\text{SC}} = \sum_{\boldsymbol{k}\in\text{MBZ}} f_{\boldsymbol{k},\eta,s}^{\dagger}(\Delta_{\boldsymbol{k};\eta})_{s,s'} f_{-\boldsymbol{k},-\eta,s'}^{\dagger} + \text{H.c.}, \quad (3.1)$$

which we decompose into singlet, $\Delta_{\boldsymbol{k};\eta}^s$, and triplet, $\boldsymbol{d}_{\boldsymbol{k};\eta}$, according to

$$\Delta_{\boldsymbol{k};\eta} = \left(\Delta_{\boldsymbol{k};\eta}^s + \boldsymbol{d}_{\boldsymbol{k};\eta}\cdot\boldsymbol{s}\right)is_y. \quad (3.2)$$

As mentioned above, we will start in the high-symmetry limit $\lambda_{\text{I}} = \lambda_{\text{R}} = 0$ and $D_0 = 0$, where the system becomes equivalent to mirror-symmetric tTLG. First note that the low-energy Bloch states at $\boldsymbol{k}$ and in valley η will have the same mirror-symmetry eigenvalue as the state at $-\boldsymbol{k}$ and in valley $-\eta$. Therefore, any pairing state in Eq. (3.1) will be even in σ_h, which is expected to be energetically most favorable [48]. Although pairing in tTLG in other representations is possible [49, 50], let us further assume that the pairing state transforms trivially under C_{3z}, which also avoids nodes in the gap function. This is motivated by the remarkably strong superconductivity in tTLG and the fact that it is enhanced when screening the Coulomb interaction [26]. The SO(3)×C_{6h} point symmetry then leaves us with [50] only two remaining superconducting states: first, there is the A_g^1 singlet, where

$$\psi_{\boldsymbol{k},\eta} = \chi_{\boldsymbol{k},\eta}, \quad \boldsymbol{d}_{\boldsymbol{k},\eta} = 0, \quad (3.3\text{a})$$

and, second, the B_u^3 triplet with

$$\psi_{\boldsymbol{k},\eta} = 0, \quad \boldsymbol{d}_{\boldsymbol{k},\eta} = \eta\chi_{\boldsymbol{k},\eta}\widehat{\boldsymbol{d}}, \quad (3.3\text{b})$$

where $\widehat{\boldsymbol{d}}$ is a three-component unit vector. In Eq. (3.3), the momentum dependence is parametrized with $\chi_{\boldsymbol{k},\eta}$ which is only required to obey $\chi_{\boldsymbol{k},\eta} = \chi_{-\boldsymbol{k},-\eta}$ and $\chi_{C_3\boldsymbol{k},\eta} = \chi_{\boldsymbol{k},\eta}$. If the interactions in the system just couple the densities of electrons in the two valleys but do not exhibit an intervalley Hund's coupling, there will be an enhanced SU(2)$_+$×SU(2)$_-$ spin symmetry. In that case, the A_g^1 and B_u^3 states will be exactly degenerate with their order parameter being parametrized by the same basis function $\chi_{\boldsymbol{k},\eta}$, as in Eq. (3.3). While there are further interesting consequences for superconductivity in the vicinity of this point [50] even without SOC, we will here focus on what happens once λ_{R} and λ_{I} are non-zero.
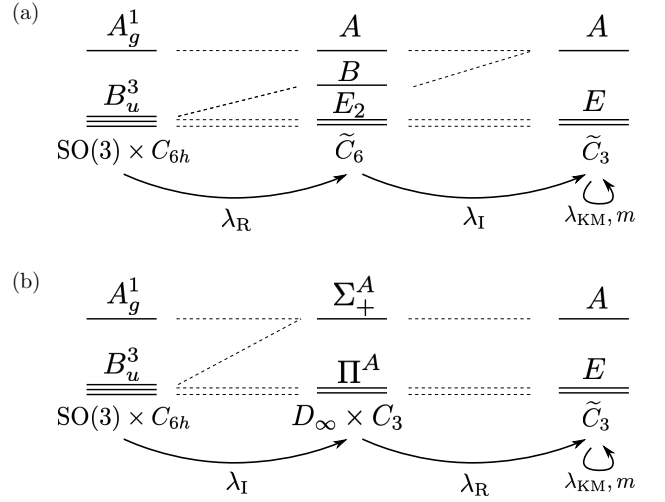

FIG. 2: Summary of superconducting states, upon (a) first turning on λ_{R} and then λ_{I} in Eq. (2.2), and vice versa (b). See Sec. III and Appendix B for details. Note that further turning on m and λ_{KM} as perturbations at the end does not change the form of the symmetry-allowed components in the superconducting order parameter, as indicated.

Let us begin by discussing the case where λ_{R} is first turned on and then λ_{I}, see Fig. 2(a). Finite λ_{R} reduces the point group SO(3)×C_{6h} to $\widetilde{C}_6$, where the tilde indicates that the elements are combinations of spatial rotations and appropriate spin rotations [formally, $\widetilde{C}_6$ is defined as the group generated by $C_{3z}^s C_{2z}^s$]. As can be worked out by investigation of the representations, the A_g^1 singlet transitions into the spin-singlet-triplet admixed A state with

$$\psi_{\boldsymbol{k},\eta} = \chi_{\boldsymbol{k},\eta}, \quad \boldsymbol{d}_{\boldsymbol{k},\eta} = \alpha_1 \begin{pmatrix} X_{\boldsymbol{k}} \\ Y_{\boldsymbol{k}} \\ 0 \end{pmatrix} + \alpha_2\,\eta \begin{pmatrix} 2X_{\boldsymbol{k}}Y_{\boldsymbol{k}} \\ X_{\boldsymbol{k}}^2 - Y_{\boldsymbol{k}}^2 \\ 0 \end{pmatrix},$$

$$(3.4)$$

where $X_{\boldsymbol{k}}$ and $Y_{\boldsymbol{k}}$ are MBZ-periodic, real-valued functions transforming as k_x and k_y under C_6. Further, $\alpha_j \in \mathbb{R}$ describe the, in general temperature dependent, admixture of the new component [transforming under E_{1u}^3 of SO(3)×C_{6h}] to the pairing states induced by finite λ_{R}.

The B_u^3 triplet splits into an E_2 doublet, which has an admixed E_{2g}^1 singlet component,

$$\begin{pmatrix} \psi_{\boldsymbol{k},\eta}^1 \\ \psi_{\boldsymbol{k},\eta}^2 \end{pmatrix} = \alpha_1 \begin{pmatrix} 2X_{\boldsymbol{k}}Y_{\boldsymbol{k}} \\ X_{\boldsymbol{k}}^2 - Y_{\boldsymbol{k}}^2 \end{pmatrix}, \quad \begin{pmatrix} \boldsymbol{d}_{\boldsymbol{k},\eta}^1 \\ \boldsymbol{d}_{\boldsymbol{k},\eta}^2 \end{pmatrix} = \eta\chi_{\boldsymbol{k},\eta} \begin{pmatrix} \boldsymbol{e}_x \\ \boldsymbol{e}_y \end{pmatrix},$$

$$(3.5)$$

and a purely spin-triplet state transforming under the one-dimensional B representation where

$$\psi_{\boldsymbol{k},\eta} = 0, \quad \boldsymbol{d}_{\boldsymbol{k},\eta} = \eta\chi_{\boldsymbol{k},\eta}\boldsymbol{e}_z. \quad (3.6)$$

Note that C_{2z}^s prohibits any singlet component in the B state, despite the presence of SOC.

Once we also turn on λ_I [and m, λ_KM in Eq. (2.2) for that matter] we further reduce the point symmetry to $\widetilde{C}_3$. The E_2 of $\widetilde{C}_3$ doublet then simply becomes the E of $\widetilde{C}_3$ doublet and mixes with the previous E_1 state (with both singlet and triplet components). The resulting order parameter is of the form

$$\begin{aligned}\begin{pmatrix}\psi^1_{\boldsymbol{k},\eta}\\\psi^2_{\boldsymbol{k},\eta}\end{pmatrix} &= \alpha_1\begin{pmatrix}2X_{\boldsymbol{k}}Y_{\boldsymbol{k}}\\X^2_{\boldsymbol{k}}-Y^2_{\boldsymbol{k}}\end{pmatrix}+\alpha_2\,\eta\begin{pmatrix}X_{\boldsymbol{k}}\\Y_{\boldsymbol{k}}\end{pmatrix},\\\begin{pmatrix}\boldsymbol{d}^1_{\boldsymbol{k},\eta}\\\boldsymbol{d}^2_{\boldsymbol{k},\eta}\end{pmatrix} &= \eta\chi_{\boldsymbol{k},\eta}\begin{pmatrix}\boldsymbol{e}_x\\\boldsymbol{e}_y\end{pmatrix}+\alpha_3\boldsymbol{e}_z\begin{pmatrix}X_{\boldsymbol{k}}\\Y_{\boldsymbol{k}}\end{pmatrix}.\end{aligned}\tag{3.7}$$

Furthermore, the A and B states merge into the singlet-triplet admixed A state of $\widetilde{C}_3$ with order parameter

$$\psi_{\boldsymbol{k},\eta}=\chi_{\boldsymbol{k},\eta},$$
$$\boldsymbol{d}_{\boldsymbol{k},\eta}=\alpha_1\begin{pmatrix}X_{\boldsymbol{k}}\\Y_{\boldsymbol{k}}\\0\end{pmatrix}+\alpha_2\,\eta\begin{pmatrix}2X_{\boldsymbol{k}}Y_{\boldsymbol{k}}\\X^2_{\boldsymbol{k}}-Y^2_{\boldsymbol{k}}\\0\end{pmatrix}+\alpha_3\eta\,\chi_{\boldsymbol{k},\eta}\boldsymbol{e}_z,$$
$$\tag{3.8a}$$

if the A state is dominant at $\lambda_\mathrm{I}=0$; if instead, the B state dominates without λ_I, Eq. (3.8a) becomes

$$\psi_{\boldsymbol{k},\eta}=\alpha_1\chi_{\boldsymbol{k},\eta},$$
$$\boldsymbol{d}_{\boldsymbol{k},\eta}=\eta\chi_{\boldsymbol{k},\eta}\boldsymbol{e}_z+\alpha_2\begin{pmatrix}X_{\boldsymbol{k}}\\Y_{\boldsymbol{k}}\\0\end{pmatrix}+\alpha_3\,\eta\begin{pmatrix}2X_{\boldsymbol{k}}Y_{\boldsymbol{k}}\\X^2_{\boldsymbol{k}}-Y^2_{\boldsymbol{k}}\\0\end{pmatrix}.$$
$$\tag{3.8b}$$

We thus see that there are two main classes of superconducting instabilities in tTLG proximity coupled to WSe_2, which are associated with the irreducible representation (IR) A and E. More specifically, by virtue of being one-dimensional, the IR A is only associated with a single superconducting state, with order parameter given in Eq. (3.8a) or Eq. (3.8b), which preserves both C^s_{3z} and Θ^s; obeying all symmetries of the normal state, this state can be fully gapped and is expected to be realized if electron-phonon coupling or the fluctuation of a time-reversal-even normal state order provides the pairing glue [51, 52]. The IR E is two-dimensional and associated with two distinct pairing states: expanding the superconducting order parameter (3.2) as

$$\Delta_{\boldsymbol{k};\eta}=\sum_{j=1,2}c_j(\psi^j_{\boldsymbol{k},\eta}+\boldsymbol{d}^j_{\boldsymbol{k},\eta}\cdot\boldsymbol{s}),\tag{3.9}$$

with complex coefficients $c_{1,2}$ and $\psi^j_{\boldsymbol{k},\eta}$, $\boldsymbol{d}^j_{\boldsymbol{k},\eta}$ given in Eq. (3.7), the first state is the nematic $E_{(1,0)}$ superconductor with $c=(1,0)^T$ (and symmetry-related configurations). It breaks C^s_{3z} but respects Θ^s and will have point nodes. The second state is the chiral $E_{(1,i)}$ superconductor with $c=(1,i)^T$ (and symmetry-related configurations), which preserves C^s_{3z} but breaks Θ^s; unless the

Fermi surface crosses the Γ, K or K' point of the MBZ, it will be fully gapped. Both E states can only be stabilized by an unconventional pairing mechanism based on fluctuations of a time-reversal-odd order parameter [51], such as spin fluctuations. As long as fluctuation corrections to mean-field [50] can be neglected in the computation of the quartic terms in the GL expansion, the chiral state will always be favored over the nematic superconductor [53].

The order in which we turned on λ_R and λ_I in our analysis above has important consequences if λ_R is sizeable but $\lambda_\mathrm{R}\gg\lambda_\mathrm{I}$. In that case, one should primarily think in terms of the three candidate states A, B, E_2 of $\widetilde{C}_6$. For instance, if B is preferred, the order parameter has the form of Eq. (3.8b) with $\alpha_{1,2,3}$ being small in λ_I. In case of E_2, the order parameter is given by Eq. (3.7) where α_1 captures an order-one singlet-triplet admixture while $\alpha_{2,3}$ are small.

To understand pairing in the opposite limit, $\lambda_\mathrm{I}\gg\lambda_\mathrm{R}$, we have studied the evolution of pairing state when first turning on λ_I before λ_R. The result is summarized graphically in Fig. 2(b) and the detailed form of the order parameters can be found in Appendix B.

IV. SYMMETRY ANALYSIS OF DIODE EFFECT

To begin our symmetry discussion of the diode effect, let us first assume that the necessary symmetry requirements are due to some additional normal-state order, i.e., interaction-induced spontaneous symmetry breaking that is already present in the normal state out of which superconductivity emerges, while no additional symmetries are spontaneously broken at the superconducting transition.

A. Candidate normal-state orders

To perform a systematic analysis of all possible normal state orders causing the ZFDE, we will start in the limit without SOC, setting all terms in Eq. (2.2) to zero. Then the system is equivalent to tTLG and we can use the set of candidate orders derived in [48], where it was shown that all order parameters listed in Table II constitute exact ground states in the chiral-flat-decoupled limit; the latter is defined by $w_0=0$ in h^t, $D_0=0$, and setting the bandwidth of the flat-bands in the mirror-even sector to zero. Tuning away from this limit will induce a multitude of different energetic contributions, removing the degeneracy between these candidate states, as detailed in Ref. 48.

More precisely, for each of these states, the mirror-even sector of the theory will be a correlated, but symmetry unbroken, semi-metal, while the mirror-odd sector with twisted-bilayer-graphene-like bandstructure exhibits the

TABLE II: Summary of candidate instabilities based on the analysis of [48]. For each state, we list a momentum-independent form of its order parameter m_j in the TBG-like bands, see Eq. (4.1), using σ_j, η_j, and s_j to denote Pauli matrices in band, valley, and spin space, respectively. We indicate how each m_j transforms under the symmetries of the system, listed in Table I. To this end, we use A (E) to denote the trivial (complex) IR of $C_{3z}^s \cong \mathbb{Z}_3$ and **1** (**3**) for the singlet (triplet) representation of the SO(3)$_s$ spin rotation group. In the column "Hund's p." we indicate the Hund's partner [48, 50] of each candidate order, i.e., the state it becomes degenerate with in the absence of SOC and intervalley Hund's interactions, leading to an enhanced SU(2)$_+\times$SU(2)$_-$ spin symmetry. Finally, the last two columns indicate which states become symmetry-equivalent, i.e., will start to mix, once λ_I or λ_R are non-zero. For convenience of the reader, this is also summarized graphically in Fig. 3.

type	m_j	SO(3)$_s$	C_{2z}^s	$C_{2z}^{s'}$	C_{3z}^s	U(1)$_v$	Θ_s	Hund's p.	$\lambda_I \neq 0$	$\lambda_R \neq 0$
SP$_\perp$/SP$_\parallel$	$\sigma_0\eta_0 s_z/\sigma_0\eta_0(s_x,s_y)$	**3**	+/−	−/±	A/E	0	−	SVP	VP/SSLP$_\parallel^+$	SLP$^-$/—
SVP$_\perp$/SVP$_\parallel$	$\sigma_0\eta_z s_z/\sigma_0\eta_z(s_x,s_y)$	**3**	−/+	+/∓	A/E	0	+	SP	—/SSLP$_\parallel^-$	SLP$^+$/—
VP	$\sigma_0\eta_z s_0$	**1**	−	−	A	0	−	—	SP$_\perp$	SSLP$_\perp^+$
SLP$^-$	$\sigma_y\eta_0 s_0$	**1**	+	+	A	0	−	—	SSLP$_\perp^+$	SP$_\perp$
SLP$^+$	$\sigma_y\eta_z s_0$	**1**	−	−	A	0	+	—	SSLP$_\perp^-$	SVP$_\perp$
SSLP$_\perp^-$/SSLP$_\parallel^-$	$\sigma_y\eta_0 s_z/\sigma_y\eta_0(s_x,s_y)$	**3**	+/−	−/±	A/E	0	+	SSLP$^+$	SLP$^+$/SVP$_\parallel$	—/—
SSLP$_\perp^+$/SSLP$_\parallel^+$	$\sigma_y\eta_z s_z/\sigma_y\eta_z(s_x,s_y)$	**3**	−/+	+/∓	A/E	0	−	SSLP$^-$	SLP$^-$/SP$_\parallel$	VP/—
IVC$^+$	$\sigma_0\eta_{x,y}s_0$	**1**	±	±	A	1	+	SIVC$^+$	SIVC$_\perp^-$	SIVC$_\perp^-$
IVC$^-$	$\sigma_y\eta_{x,y}s_0$	**1**	±	±	A	1	−	SIVC$^-$	SIVC$_\perp^+$	SIVC$_\perp^+$
SIVC$_\perp^+$/SIVC$_\parallel^+$	$\sigma_0\eta_{x,y}s_z/\sigma_0\eta_{x,y}(s_x,s_y)$	**3**	±/∓	∓/±	A/E	1	−	IVC$^+$	IVC$^-$/—	IVC$^-$/—
SIVC$_\perp^-$/SIVC$_\parallel^-$	$\sigma_y\eta_{x,y}s_z/\sigma_y\eta_{x,y}(s_x,s_y)$	**3**	±/∓	∓/±	A/E	1	+	IVC$^-$	IVC$^+$/—	IVC$^+$/—

respective order parameters Φ_j, coupling to the electrons as

$$\Delta H_0 = \sum_{\boldsymbol{k}\in\text{MBZ}} b_{\boldsymbol{k}}^\dagger m_j b_{\boldsymbol{k}}\,\Phi_j. \qquad (4.1)$$

In Eq. (4.1), m_j are matrices in valley, spin, and band-space; the latter is spanned by the conduction (just above the charge-neutrality point) and valence (just below it) flat-bands of twist-bilayer graphene. The associated field operators are $b_{\boldsymbol{k};p,\eta,s}^\dagger$ which create Bloch electrons in the mirror-even conduction ($p = +$) or valence ($p = -$) flat band, in valley η and spin s. The m_j for each of these candidate orders can be found in the second column of Table II, where we denote Pauli matrices in band space by σ_j (index $p = \pm$ above). Note that we use this form of m_j simply to characterize the different phases, in particular their symmetries, which can also be found in Table II, and that the energetically most favorable version of each phase will have a $\boldsymbol{k}$-dependent order parameter that mixes different bands [48].

Our main focus here will be on the impact of the SOC terms λ_I and λ_R. Both of these terms will reduce the symmetries of the system, see Sec. II B and Table I, with two crucial consequence: first, all spin-polarized orders, which at $\lambda_I = \lambda_R = 0$ belong to the three-dimensional IR of SO(3)$_s$ split into two different orders, associated with in-plane ($\parallel$) and out-of-plane spin polarizations ($\perp$). This increases the number of physically distinct candidate phases compared to tTLG [48]. At the same time, the reduction of symmetries reduces the number of IRs

and previously distinct orders transform identically under all symmetries of the system. This means that they can mix and should be formally viewed as the same phase, reducing the number of distinct candidate orders. For instance, out-of-plane spin polarization (SP$_\perp$ in Table II) and valley polarization (VP), while physically distinct for $\lambda_I = 0$ due to their behavior under C_{2z}^s, become identical once Ising SOC is non-zero, $\lambda_I \neq 0$. Which states become equivalent once λ_R or λ_R is turned on is summarized in the last two columns in Table II.

Since the "evolution" of the candidate orders is quite complex, we have also illustrated it graphically in Fig. 3. Note that U(1)$_v$ symmetry is always preserved in our description which is why intervalley coherent (IVC) states [breaking U(1)$_v$] cannot mix with states that preserve it. As can be seen in Fig. 3(a), we end up with only four distinct U(1)$_v$-preserving phases once λ_I and λ_R are non-zero. However, the diagram contains more relevant information if one of λ_I, λ_R is small. For instance, if λ_R is small and only provides a tiny perturbation to the energetics, while λ_I is large (compared to the energetic differences between the candidate orders in Table II at $\lambda_I = \lambda_R = 0$, i.e., of order of a couple of meV [48]), Fig. 3(a) implies that one should not distinguish between VP and SP$_\perp$, as they will generically mix strongly. However, there is still an important distinction to be made between VP = SP$_\perp$ with a little bit of SSLP$_\perp^+$ = SLP$^-$ admixed and vice versa [primarily SSLP$_\perp^+$ = SLP$^-$ with a little bit of VP = SP$_\perp$]. If also λ_R is large, this distinction will become irrelevant. As can be seen in Fig. 3(b),
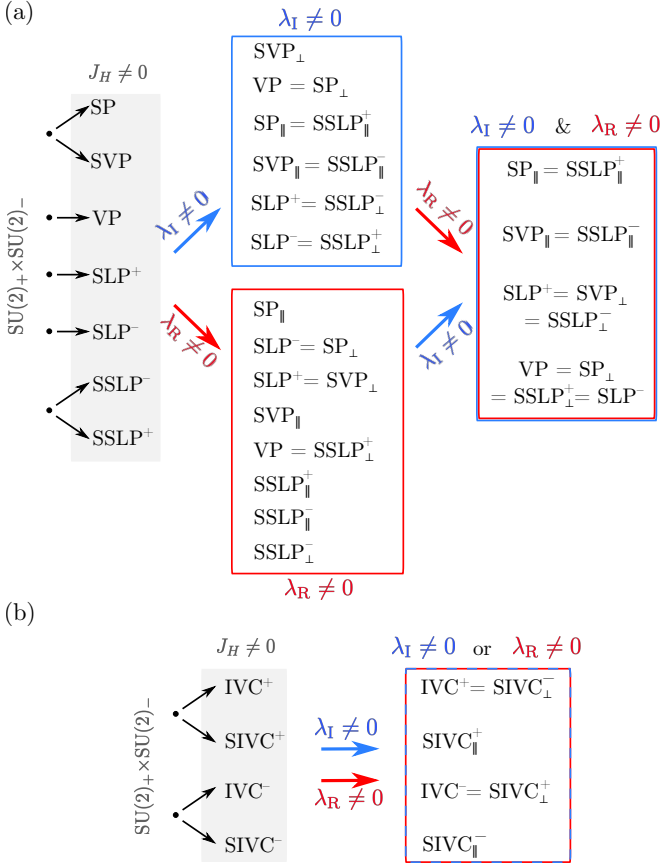
FIG. 3: Evolution of normal state orders in Table II upon turning on the SOC terms λ_R and λ_I. As neither of these terms break the valley $U(1)_v$ symmetry, we can group these states into (a) $U(1)_v$-preserving and (b) intervalley coherent (IVC) phases.

only four distinct IVC order are possible if λ_R or λ_I or both are large.

B. Zero-field diode effect

We will next discuss whether a superconducting diode effect is possible by symmetry in the presence of any of the different normal state orders in Table II and Fig. 3. We will here make the natural assumption that the superconductor that emerges out of this symmetry-broken normal state does not spontaneously break additional symmetries. The diode effect for the symmetry-breaking superconductors in the IR E, see Sec. III, will be postponed to Sec. IV D below.

To formalize the discussion, let us denote the magnitude of the critical current density for a current along the in-plane direction $\hat{n}$ by $J_c(\hat{n})$. The system exhibits a diode effect if there is some direction $\hat{n}$ for which the current asymmetry,

$$\delta J_c(\hat{n}) := J_c(\hat{n}) - J_c(-\hat{n}), \qquad (4.2)$$

is non-zero. Inspection of the symmetries in Table I, shows that the presence of at least one of the symmetries Θ, Θ^s, C_{2z}, C_{2z}^s, $C_{2z}^{s'}$, I, without or combined with a $U(1)_v$ transformation, implies that $J_c(\hat{n}) = J_c(-\hat{n})$ and no ZFDE is present.

It is straightforward to analyze for each of the 17 candidate orders defined in Table II whether any of these symmetries is present as a function of whether any combination of λ_I, λ_R, and β is non-zero. This allows us to deduce whether a ZFDE is possible at all and, if yes, which of λ_I, λ_R, β the current asymmetry δJ_c has to be proportional to. For instance, $SP_\perp$ preserves C_{2z}^s as long as λ_I vanishes. As such, the diode effect can only be present if $\lambda_I \neq 0$ and $\delta J_c(\hat{n}) \propto \lambda_I$. For VP this is different, as it breaks all of the above-mentioned symmetries and hence exhibits a diode effect even if $\lambda_I = \lambda_R = \beta = 0$. For any of the IVC states in Table II, no diode effect is possible for any value of λ_I, λ_R, and β since, in all cases, a combination of $U(1)_v$ and Θ^s remains a symmetry. In fact, out of 17 candidate orders only the six states listed in Table III are consistent with a ZFDE, with $\delta J_c(\hat{n})$ as indicated in the third column. We reiterate that some of these six states further become equivalent once λ_I or λ_R become sizeable as shown in Fig. 3. In the limit where both λ_I or λ_R are large (of order of a few meV [48], which might very well be the case [31, 35]), these six states decay into only two distinct phases (above and below the horizontal line in Table II).

To be able to distinguish further between the remaining six microscopic candidate orders in Table II driving the diode effect, let us analyze whether and under which conditions they can be trained by a magnetic field. An order parameter m_j can be trained linearly by an external field $\mathcal{B}$, if and only if a linear coupling, $c(\lambda_I, \lambda_R, \beta)\mathcal{B}\Phi_j$, between the associated Φ_j in Eq. (4.1) and $\mathcal{B}$ is allowed in the free energy. Whether c can be non-zero and its behavior for small λ_I, λ_R, and β can be deduced by symmetry. For $\mathcal{B}$ being either in-plane or out-of-plane Zeeman or orbital magnetic field, we list the respective $c(\lambda_I, \lambda_R, \beta)$ in the last four columns in Table III for all six states with a diode effect. Most strikingly, if β vanishes, the four states above the horizontal line (the two below it) cannot be trained by an in-plane (out-of-plane) magnetic field. As we expect β to be rather weak in the samples of Ref. 20, where the ZFDE can be trained much more effectively by an out-of-plane magnetic field, the four states above the horizontal line are much more likely behind the observed diode effect in tTLG on WSe$_2$.

To learn more about the underlying mechanism of the diode effect, we also investigate under which conditions the $\hat{n}$-dependence of the critical current $J_c(\hat{n})$ is three-fold symmetric, $J_c(\hat{n}) = J_c(C_{3z}\hat{n})$, for all of the above six scenarios with a diode effect. The dependence of the associated asymmetry $J_c(\hat{n}) - J_c(C_{3z}\hat{n})$ for small λ_I, λ_R, β is given in the fourth column of Table III. It reveals

TABLE III: Out of the in total 17 different states in Table II, only the following six can lead to a diode effect. However, note that the first four of these state (the last two), above (below) the vertical line, have the same symmetries as long as $\lambda_I, \lambda_R \neq 0$ and, hence, mix and formally constitute the same phase, see also Fig. 3. We list not only which of λ_I, λ_R have to be non-zero for a diode effect, $J_c(\hat{n}) \neq J_c(-\hat{n})$, but also whether the critical current is C_{3z} symmetric. Finally, the last four columns indicate whether the underlying normal-state order and, hence, the diode effect can be trained by an in-plane (out-of-plane) Zeeman $B_\parallel^Z$ ($B_\perp^Z$) and orbital magnetic field $B_\parallel^O$ ($B_\perp^O$). As with the critical current, we list which of $\lambda_I, \lambda_R, \beta$ the respective coupling has to be proportional to. Here $(D_0, \lambda_I, \lambda_R)$ indicates that one of the three is sufficient.

normal state		critical current		trainability			
type	m_j	$J_c(\hat{n}) - J_c(-\hat{n})$	$J_c(\hat{n}) - J_c(C_{3z}\hat{n})$	$B_\perp^Z$	$B_\parallel^Z$	$B_\perp^O$	$B_\parallel^O$
$\mathrm{SP}_\perp$	$\sigma_0\eta_0 s_z$	$\propto \lambda_I$	$\propto \beta$	$\neq 0$	$\propto \beta\lambda_I\lambda_R$	$\propto \lambda_R$	$\propto \beta\lambda_I$
VP	$\sigma_0\eta_z s_0$	$\neq 0$	$\propto \beta$	$\propto \lambda_I$	$\propto \beta\lambda_R$	$\propto \lambda_I\lambda_R$	$\propto (D_0, \lambda_I, \lambda_R)\beta$
$\mathrm{SSLP}_\perp^+$	$\sigma_y\eta_z s_z$	$\propto \lambda_R$	$\propto \beta$	$\propto \lambda_I$	$\propto \beta\lambda_R$	$\propto \lambda_I$	$\propto \beta\lambda_R$
SLP^-	$\sigma_y\eta_0 s_0$	$\propto \lambda_R\lambda_I$	$\propto \beta$	$\propto \lambda_R$	$\propto \beta\lambda_I$	$\propto (D_0, \lambda_I, \lambda_R)$	$\propto \beta\lambda_I\lambda_R$
$\mathrm{SP}_\parallel$	$\sigma_0\eta_0(s_x, s_z)$	$\propto \lambda_R$	$\propto \lambda_R$	$\propto \beta\lambda_I\lambda_R$	$\neq 0$	$\propto \beta\lambda_I\lambda_R$	$\propto \lambda_R$
$\mathrm{SSLP}_\parallel^+$	$\sigma_y\eta_z(s_x, s_y)$	$\propto \lambda_R\lambda_I$	$\propto \lambda_R$	$\propto \beta\lambda_R$	$\propto \lambda_I$	$\propto \beta\lambda_R$	$\propto \lambda_I\lambda_R$

another crucial distinction between the first four and the last two candidate order parameters, that might be used in future experiment to probe the underlying physics: while $J_c(\hat{n})$ will be three-fold symmetric (unless $\beta \neq 0$, where C_{3z} is trivially broken by the lattice or if it is broken spontaneously) for the first four states, it will not be three-fold invariant for the last two as long as $\lambda_R \neq 0$. We emphasize that this distinction has crucial consequences for the diode effect: in the three-fold symmetric case, the current asymmetry $\delta J_c(\hat{n})$ in Eq. (4.2) is required to have six zeros as $\hat{n}$ rotates by 2π—a property that will not change if that rotational symmetry is only slightly broken by finite β; without that constraint, it is only required to have two. We will see examples of both in our explicit calculations in Sec. V C below.

C. Field-induced diode effect

Although the main focus of this work is on the ZFDE, we briefly comment on the Zeeman-field induced diode effect, which has already been studied previously in two-dimensional spin-orbit coupled systems [3–5]. Upon noting that the in-plane Zeeman-field and the $\mathrm{SP}_\parallel$ order parameter in Table II transform identically under all symmetries of the system, we can immediately read off from Table III that Rashba SOC coupling is required to induce a diode effect with an in-plane Zeeman field for pairing in the IR A and without additional normal-state order [$\Phi_j = 0$ in Eq. (4.1)].

Experimentally, it is found that the sample displaying the ZFDE does not exhibit a sizeable field-induced diode effect [20] for in-plane fields. As we will demonstrate in Sec. V D below, this might be understood as a consequence of the additional Ising SOC. Note that the in-plane orbital coupling—associated with Peierls phases

in the interlayer hopping—is not expected to yield a large contribution to the diode effect either since its impact on the current asymmetry δJ_c in Eq. (4.2) vanishes (approximately) when the mirror symmetry σ_h is (approximately) conserved. This follows from the observation that the in-plane orbital coupling (in-plane current) is odd (even) under σ_h.

While the sample with ZFDE can be trained efficiently with out-of-plane fields, which makes the notion of a field-induced diode effect for this sample ill-defined for fields perpendicular to the plane, Ref. 20 also presents data for a sample without ZFDE. This sample shows a weak diode effect in the presence of a small out-of-plane field. Since an out-of-plane Zeeman field transforms as $\mathrm{SP}_\perp$, we see in Table III that it will induce a diode effect as long as λ_I is non-zero (while the orbital-coupling-induced diode effect will likely be sub-leading as its impact on the diode effect has to be proportional to $\lambda_I\lambda_R$). The behavior of the critical current of this sample is therefore consistent with a sizeable λ_I and indicates that superconductivity does not coexist with any of the phases in Table III (in particular, those where $\delta J_c \neq 0$ for $\lambda_R = 0$).

D. Diode effect without normal-state order

So far, we have assumed that the necessary symmetry-requirements, including broken time-reversal symmetry, stem from the normal state while the superconductor preserves all normal-state symmetries (pairing in IR A in Fig. 2). However, we have seen in Sec. III that the other pairing channel, associated with the IR E in Fig. 2, does allow for a superconducting state, denoted by $E_{(1,i)}$ above, that spontaneously breaks time-reversal symmetry. In this case, even without any normal-state order, $\Phi_j = 0$ in Eq. (4.1), the resulting superconducting phase

breaks all symmetries in Table I (Θ, Θ^s, C_{2z}, C_{2z}^s, $C_{2z}^{s'}$, I) which have to be broken for a ZFDE.

We first note that this state will still not lead to a ZFDE, if the superconductor always reaches the global energetic minimum in the current-carrying state; this is discussed and demonstrated in Appendix C and is a direct consequence of the time-reversal symmetry of the normal state. To understand why this does not always have to be the case, let us consider the gauge-invariant quantity

$$\mathcal{C} := i\frac{1}{V} \int \mathrm{d}\boldsymbol{x} \left(c_1^* c_2 - c_2^* c_1\right) \tag{4.3}$$

with c_j introduced in Eq. (3.9) which we here also allow to be spatially varying; the integral in Eq. (4.3) is over the entire system (with volume V). Importantly, $\mathcal{C}$ is odd under Θ_s but invariant under C_{3z} and can thus be thought of as a composite order parameter measuring the broken time-reversal symmetry (absence thereof) in the $E_{(1,i)}$ ($E_{(1,0)}$) state. Note that $\langle C \rangle \neq 0$ does not break any continuous symmetry and, in particular, does not require superconducting phase coherence; instead, it is an Ising-like order parameter that can develop long-range order at a finite temperature T^*. In particular in the limit where T^* is significantly larger than T_c, we can think of $\mathcal{C}$ as a magnetic order parameter, similar to m_j in Eq. (4.1), defining a "vestigial" [54] magnetic phase (for $T_c < T < T^*$) associated with the $E_{(1,i)}$ superconductor at lower $T < T_c$. If $\mathcal{C}$ exhibits a fixed sign when measuring the critical current, we can indeed obtain a diode effect (see Appendix C). We point out that this mechanism of the diode effect is related to the one recently discussed in [55] for chiral p-wave pairing, to understand the asymmetric I-V characteristics of the 3-K phase in eutectic samples of Sr_2RuO_4 [56]. A crucial difference is that, in our case, no additional symmetry-breaking boundary conditions are required due to the reduced symmetry of tTLG on WSe$_2$.

In agreement with experiment [20], the intrinsic ZFDE of the $E_{(1,i)}$ state of tTLG/WSe$_2$ can (cannot) be trained linearly with a perpendicular (parallel) Zeeman or orbital magnetic field if $\beta = 0$. This follows by noting that $\mathcal{C}$ in Eq. (4.3) can couple linearly to out-of-plane but not to in-plane magnetic fields (due to C_{3z}^s). Furthermore, in this scenario, the vestigial phase associated with non-zero $\mathcal{C}$ is a possible origin of, or at least provides an additional contribution to, the enhanced transverse resistance above T_c seen in experiment [20]. Nonetheless, the currently available experimental data is more naturally consistent with pairing in the IR A together with a time-reversal-symmetry-breaking normal-state order m_j: so far, clear experimental signatures of magnetism in various graphene moiré systems have been reported, see, e.g., [57–59], while a superconducting order parameter in a non-trivial IR of the spatial point group has not

been clearly identified to date. Furthermore, this unconventional pairing state is expected to be more fragile against disorder on the moiré scale than the A state [52]. For these reasons, we will focus on superconducting order parameters in the IR A in our explicit calculations in the following sections.

V. MODEL CALCULATIONS

In this section we present the general Ginzburg-Landau formalism which allows for the diode effect, finite $\boldsymbol{q}$ pairing and nematicity, to be directly computed. To understand the salient features, we begin with a patch theory. We move onto 2D toy models which provide a description accounting for the entire MBZ. Finally, we perform direct computations for the full tTLG theory (2.1).

A. General formalism

As we have argued above, valley polarization (even without SOC), which is symmetry-equivalent to out-of-plane spin polarization in the presence of Ising SOC, is the most natural cause of the reduced symmetry in the normal state that ultimately leads to the diode effect. To capture both of these scenarios simultaneously and in a way that identifies the key ingredients for the diode effect, we will neglect SOC for now and assume that there is an imbalance in the occupations of the different valleys. Let us for concreteness also first assume that this imbalance is not too strong such that Cooper pairs of electrons still form between electrons of different valleys ("intervalley pairing"). We will see that, for the purposes of computing the current (diode effect), accounting for "intra-valley" pairing and/or SOC, follows immediately from the expressions provided here.

To be concrete, consider the Hamiltonian

$$H = \sum_{\boldsymbol{k}} f_{\boldsymbol{k},\eta,s}^\dagger E_{\boldsymbol{k},\eta} f_{\boldsymbol{k},\eta,s}$$
$$- \frac{g}{2} \sum_{\boldsymbol{k},\boldsymbol{k'},\boldsymbol{q}} f_{\boldsymbol{k}+\boldsymbol{q},\eta,s}^\dagger f_{\boldsymbol{k'}-\boldsymbol{q},\eta',s'}^\dagger f_{\boldsymbol{k'},\eta',s'} f_{\boldsymbol{k},\eta,s}, \tag{5.1}$$

where $f_{\boldsymbol{k},\eta,s}$ and $f_{\boldsymbol{k},\eta,s}^\dagger$ are annihilation and creation operators of electrons of spin s, valley η, in the low-energy bands crossing the Fermi level in the vicinity of $\boldsymbol{k}$. The band energies in valley η are denoted by $E_{\boldsymbol{k},\eta}$; without valley polarization, we have $E_{\boldsymbol{k},+} = E_{-\boldsymbol{k},-}$ as follows from time-reversal symmetry. The simplest form to describe valley polarization is to introduce two different chemical potentials, $E_{\boldsymbol{k},\eta} = \epsilon_{\eta \cdot \boldsymbol{k}} - \mu_\eta$, but we will keep it more general here. As there is no intervalley Hund's coupling, the model in Eq. (5.1) is invariant under independent spin-rotations in the two valleys forming the group $SU(2)_+ \times SU(2)_-$.

Performing a mean-field decoupling in the intervalley channel, we obtain

$$H = \sum_{\boldsymbol{k}} f_{\boldsymbol{k},\eta,s}^\dagger E_{\boldsymbol{k},\eta} f_{\boldsymbol{k},\eta,s} + \frac{1}{g} \sum_{\boldsymbol{q}} \mathrm{tr}\left[\Delta_{\boldsymbol{q}}^\dagger \Delta_{\boldsymbol{q}}\right]$$
$$+ \sum_{\boldsymbol{k},\boldsymbol{q}} \left[f_{\boldsymbol{k}+\boldsymbol{q},+,s}^\dagger (\Delta_{\boldsymbol{q}})_{s,s'} f_{-\boldsymbol{k},-,s'}^\dagger + \mathrm{H.c.}\right]. \quad (5.2)$$

Here, the 2×2 matrix $\Delta_{\boldsymbol{q}}$ is the superconducting order parameter, which can be expanded in singlet and triplet as

$$\Delta_{\boldsymbol{q}} = \left(\Delta_{\boldsymbol{q}}^s s_0 + \boldsymbol{d}_{\boldsymbol{q}} \cdot \boldsymbol{s}\right) i s_y, \quad (5.3)$$

similar to Eq. (3.2). By integrating out the fermions, it is straightforward to derive the associated Ginzburg-Landau expansion which becomes (with number of sites N in the system)

$$\mathcal{F} \sim \sum_{\boldsymbol{q}} a_{\boldsymbol{q}} \mathrm{tr}\left[\Delta_{\boldsymbol{q}}^\dagger \Delta_{\boldsymbol{q}}\right] + \mathcal{O}(\Delta^4), \ a_{\boldsymbol{q}} = \frac{1}{g} - \Gamma(\boldsymbol{q}), \quad (5.4)$$

$$\Gamma(\boldsymbol{q}) = \frac{1}{2N} \sum_{\boldsymbol{k}\in\mathrm{MBZ}} \frac{\tanh\left(\frac{E_{\boldsymbol{k}+\frac{\boldsymbol{q}}{2},+}}{2T}\right) + \tanh\left(\frac{E_{-\boldsymbol{k}+\frac{\boldsymbol{q}}{2},-}}{2T}\right)}{E_{\boldsymbol{k}+\frac{\boldsymbol{q}}{2},+} + E_{-\boldsymbol{k}+\frac{\boldsymbol{q}}{2},-}}.$$

Since $\mathrm{tr}\left[\Delta_{\boldsymbol{q}}^\dagger \Delta_{\boldsymbol{q}}\right] = 2(|\Delta_{\boldsymbol{q}}^s|^2 + \boldsymbol{d}_{\boldsymbol{q}}^\dagger \boldsymbol{d}_{\boldsymbol{q}})$, we see that singlet and triplet are degenerate, which is a consequence of the aforementioned enhanced $\mathrm{SU}(2)_+ \times \mathrm{SU}(2)_-$ spin symmetry.

To understand the relation to the diode effect, let us note that gauge invariance demands that a homogeneous vector potential $\boldsymbol{A}$ enters as

$$\mathcal{F} \sim \sum_{\boldsymbol{q}} a_{\boldsymbol{q}-2e\boldsymbol{A}} \, \mathrm{tr}\left[\Delta_{\boldsymbol{q}}^\dagger \Delta_{\boldsymbol{q}}\right]$$
$$+ \sum_{\boldsymbol{q}_1,\boldsymbol{q}_2,\boldsymbol{q}_3,\boldsymbol{q}_4} \delta_{\boldsymbol{q}_1+\boldsymbol{q}_3,\boldsymbol{q}_2+\boldsymbol{q}_4} \big\{ b_1 \mathrm{tr}\left[\Delta_{\boldsymbol{q}_1}^\dagger \Delta_{\boldsymbol{q}_2}\right] \mathrm{tr}\left[\Delta_{\boldsymbol{q}_3}^\dagger \Delta_{\boldsymbol{q}_4}\right]$$
$$+ b_2 \mathrm{tr}\left[\Delta_{\boldsymbol{q}_1}^\dagger \Delta_{\boldsymbol{q}_2} \Delta_{\boldsymbol{q}_3}^\dagger \Delta_{\boldsymbol{q}_4}\right] \big\}, \quad (5.5)$$

where e is the electron charge. Here we have also added terms quartic in the order parameter [50], neglecting the momentum dependence of b_1 and b_2.

Finding the minimum of $\mathcal{F}$ for $\boldsymbol{A} = 0$ is straightforward: let $\boldsymbol{q}_0$ be the momentum of (one of) the minimum (minima) of $a_{\boldsymbol{q}}$ and $a_{\boldsymbol{q}_0} < 0$; restricting the analysis to single-$\boldsymbol{q}$ superconducting order parameters, we then get $\Delta_{\boldsymbol{q}} = \delta_{\boldsymbol{q},\boldsymbol{q}_0} \Psi \hat{\Delta}$ with $\Psi \in \mathbb{C}$ and $\mathrm{tr}[\hat{\Delta}^\dagger \hat{\Delta}] = 1$. Depending on whether $b_2 > 0$ or $b_2 < 0$ we get $\hat{\Delta} = \sigma_0/\sqrt{2}$ or $\hat{\Delta} = (\sigma_0 + \sigma_z)/2$, which corresponds to singlet/unitary triplet or singlet-triplet/non-unitary triplet, respectively; we refer to [50] for a detailed discussion of these superconducting states in the vicinity of the $\mathrm{SU}(2)_+ \times \mathrm{SU}(2)_-$-symmetric point we focus on here. Furthermore, it holds $|\Psi|^2 = -a_{\boldsymbol{q}_0}/(2b)$ with $b = b_1 + b_2/2$ for $b_2 > 0$ and $b = b_1 + b_2$ for $b_2 < 0$.

In real space, the order parameter is $\Delta(\boldsymbol{x}) = \Psi e^{i\boldsymbol{q}_0 \cdot \boldsymbol{x} + i\phi} \hat{\Delta}$. For constant ϕ, the equilibrium condensate forms at a wavevector $\boldsymbol{q}_0$ found from

$$\partial_{\boldsymbol{q}} a_{\boldsymbol{q}}\big|_{\boldsymbol{q}_0} = 0, \ \text{and} \ \det \partial_{q_i} \partial_{q_j} a_{\boldsymbol{q}}\big|_{\boldsymbol{q}_0} > 0. \quad (5.6)$$

A supercurrent is imposed by taking a finite sample and setting a phase gradient, i.e., we generalize to spatially varying phases, $\phi \to \phi(\boldsymbol{x})$, in $\Delta(\boldsymbol{x})$ and impose twisted boundary conditions in ϕ. The simplest scenario is to take $\phi(\boldsymbol{x}) = \delta\boldsymbol{q} \cdot \boldsymbol{x}$, for some fixed $\delta\boldsymbol{q}$. In this *nonequilibrium* case, the condensate forms at effective wavevector $\boldsymbol{q} = \boldsymbol{q}_0 + \delta\boldsymbol{q}$, since $\Delta(\boldsymbol{x}) = \Psi e^{i(\boldsymbol{q}_0 + \delta\boldsymbol{q}) \cdot \boldsymbol{x}} \hat{\Delta}$. The definition of current follows from $\boldsymbol{J} = -\partial_{\boldsymbol{A}} \mathcal{F}\big|_{\boldsymbol{A}=\boldsymbol{0}} = 2e|\Psi|^2 \partial_{\boldsymbol{q}} a_{\boldsymbol{q}}$, with charge $2e$ (see [3] for a microscopic derivation of the current). Using the saddle point solution, $|\Psi|^2 = -a_{\boldsymbol{q}}/(2b)$, we arrive at

$$\boldsymbol{J}(\boldsymbol{q}) = -e\Theta(-a_{\boldsymbol{q}}) a_{\boldsymbol{q}} \partial_{\boldsymbol{q}} a_{\boldsymbol{q}}/b. \quad (5.7)$$

Here $\Theta(...)$ is a step-function ensuring that the saddle point condition $|\Psi|^2 = -a_{\boldsymbol{q}}/(2b) \geq 0$ is satisfied.

The critical current $J_c(\hat{n})$ along the direction $\hat{n}$ is now simply given by the maximum magnitude of $\boldsymbol{J}(\boldsymbol{q})$ for $\boldsymbol{q} \in \mathrm{MBZ}$ which points along $\hat{n}$. From this, we conclude that $J_c(\hat{n}) = J_c(-\hat{n})$, and therefore no diode effect, if

$$\exists \boldsymbol{q}_0 : \ \Gamma(\boldsymbol{q} - \boldsymbol{q}_0) = \Gamma(-\boldsymbol{q} - \boldsymbol{q}_0). \quad (5.8)$$

We emphasize that $\boldsymbol{q}_0$ does not have to be $\boldsymbol{0}$.

An instructive, albeit fine-tuned, example is $E_{\boldsymbol{k},+} = \epsilon_{\boldsymbol{k}+\boldsymbol{Q}/2} - \mu$, $E_{\boldsymbol{k},-} = \epsilon_{-\boldsymbol{k}-\boldsymbol{Q}/2} - \mu$ which also has broken time-reversal and C_{2z} symmetry since $E_{\boldsymbol{k},+} \neq E_{-\boldsymbol{k},-}$, as long as $\boldsymbol{Q} \notin \mathrm{RML}$. From Eq. (5.4), we get

$$\Gamma(\boldsymbol{q}) = \frac{1}{2N} \sum_{\boldsymbol{k}\in\mathrm{MBZ}} \left\{ \frac{\tanh\left(\frac{1}{2T}(\epsilon_{\boldsymbol{k}+\frac{\boldsymbol{q}+\boldsymbol{Q}}{2}} - \mu)\right)}{\epsilon_{\boldsymbol{k}+\frac{\boldsymbol{q}+\boldsymbol{Q}}{2}} + \epsilon_{\boldsymbol{k}-\frac{\boldsymbol{q}+\boldsymbol{Q}}{2}} - 2\mu} \right.$$
$$\left. + \frac{\tanh\left(\frac{1}{2T}(\epsilon_{\boldsymbol{k}-\frac{\boldsymbol{q}+\boldsymbol{Q}}{2}} - \mu)\right)}{\epsilon_{\boldsymbol{k}+\frac{\boldsymbol{q}+\boldsymbol{Q}}{2}} + \epsilon_{\boldsymbol{k}-\frac{\boldsymbol{q}+\boldsymbol{Q}}{2}} - 2\mu} \right\}. \quad (5.9)$$

Clearly, $\Gamma(\boldsymbol{q})$ in Eq. (5.9) obeys Eq. (5.8) with $\boldsymbol{q}_0 = \boldsymbol{Q}$ and, hence, cannot exhibit a diode effect. Nonetheless, $\widetilde{\Gamma}(\boldsymbol{q}') := \Gamma(\boldsymbol{q}' - \boldsymbol{Q})$ is exactly equivalent to the Γ of the time-reversal symmetric situation with $E_{\boldsymbol{k},+} = E_{-\boldsymbol{k},-} = \epsilon_{\boldsymbol{k}} - \mu$. As such, we know that $\widetilde{\Gamma}(\boldsymbol{q}')$ is maximal for $\boldsymbol{q}' = 0$ and the resulting pairing occurs at finite wavevector $\boldsymbol{q}_0 = \boldsymbol{Q}$.

Finally, to account for the cases with (i) strong SOC, or (ii) intravalley pairing, we allow for arbitrary quantum numbers α in Eq. (5.4); in case (i), the Bloch states at the Fermi surface can be labelled uniquely by their valley quantum number, $\alpha = \eta$, and exhibit momentum-dependent spin orientations, while $\alpha = \{\eta, s\}$ for case (ii). The dependence on index α enters via the particle-particle susceptibility, and in principle, the pairing interaction strength, g. As we derive in Appendix E, the
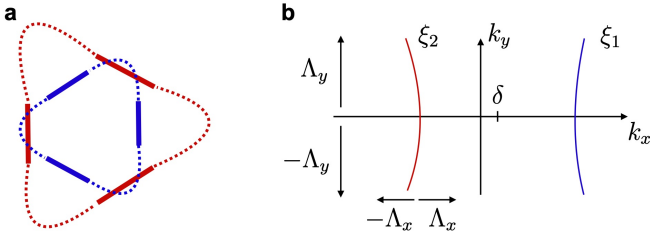
FIG. 4: Definition of patch theory. (a) Schematic Fermi surfaces from each valley (red and blue), under a valley polarizing perturbation. Bold, straight segments correspond to the patches. (b) Definition of the effective band energies about a single patch.

resulting $a_{\boldsymbol{q}}$ in Eq. (5.4) has the same form as above,

$$a_{\boldsymbol{q}} = \frac{1}{g} - \Gamma(\boldsymbol{q}), \tag{5.10}$$

$$\Gamma(\boldsymbol{q}) = \frac{1}{2N} \sum_{\boldsymbol{k} \in \text{MBZ}} \frac{\tanh\left(\frac{\xi_{\boldsymbol{k}+\frac{\boldsymbol{q}}{2},\alpha}}{2T}\right) + \tanh\left(\frac{\xi_{-\boldsymbol{k}+\frac{\boldsymbol{q}}{2},\alpha'}}{2T}\right)}{\xi_{\boldsymbol{k}+\frac{\boldsymbol{q}}{2},\alpha} + \xi_{-\boldsymbol{k}+\frac{\boldsymbol{q}}{2},\alpha'}},$$

with the only difference that $E_{\boldsymbol{k},\eta}$ are replaced by the band energies $\xi_{\boldsymbol{k},\alpha}$ of the appropriate quantum numbers [cf. Eqs. (E3) and (E4)].

B. Patch theory

Having established the general formalism, we begin our analysis with a simple patch-theory description as it allows for a particularly transparent analysis. For now, we neglect SOC, and treat singlet and triplet pairing on equal footing. Below in Sec. VD, SOC and the Fermi surfaces of the full continuum model (2.1) will be taken into account.

Having in mind tTLG, we consider pairing of states at $\{\boldsymbol{k}, \eta\}$ and $\{-\boldsymbol{k}, -\eta\}$, whereby the Fermi surfaces at each valley are C_{3z} symmetric, and we account for valley polarization. For the purpose of modelling, we consider the schematic Fermi surfaces shown in Fig. 4(a). Due to (approximate) nesting, the particle-particle susceptibility receives the largest contribution for momenta in the vicinity of the three (nearly) parallel segments. Based on this observation, we may reduce the full MBZ down to these three patches. For the single patch shown in Fig. 4(b), we have (with $\delta q_x = q_x - \delta$)

$$\Gamma^p(\boldsymbol{q}) = \int_{-\Lambda_y}^{\Lambda_y} \frac{\mathrm{d}k_y}{2\pi} \int_{-\Lambda_x}^{\Lambda_x} \frac{\mathrm{d}\delta k_x}{4\pi} \frac{\tanh\left[\frac{\xi_1}{2T}\right] + \tanh\left[\frac{\xi_2}{2T}\right]}{\xi_1 + \xi_2},$$
$$\xi_1 = v(\delta k_x + \delta q_x/2) - \alpha_+(k_y + q_y/2)^2,$$
$$\xi_2 = v(\delta k_x - \delta q_x/2) - \alpha_-(k_y - q_y/2)^2. \tag{5.11}$$

In this description, valley polarization enters both as the finite average momentum δ of the red and blue segments

as well as in form of the imbalance $\alpha_+ - \alpha_-$ of the curvature of the Fermi surfaces, see Fig. 4. Taking all three patches, we arrive at

$$\Gamma(\boldsymbol{q}) = \sum_{j=-1,0,1} \Gamma^p\left(R(2\pi j/3)\boldsymbol{q}\right), \tag{5.12}$$

where $R(\varphi)$ rotates two-dimensional vectors by angle φ. To obtain a simplified intuitive understanding for the conditions for (i) diode effect and (ii) finite-momentum pairing and nematic superconductivity, let us expand Γ^p in Eq. (5.11) as

$$\Gamma^p(\boldsymbol{q}) \sim \Gamma_0 - \sum_{n=1}^{4} a_n(q_x - \delta)^n - cq_y^2. \tag{5.13}$$

It is deduced from Eq. (5.11), that the coefficients $a_1, a_3 \propto \alpha_+ - \alpha_-$. Explicit expressions for a_n and c are presented in Appendix D. Consequently, to leading order, a_1, a_3, and δ will vary linearly with valley polarization. Using $\nu \in [-1, 1]$ as a dimensionless measure of the valley polarization, we write $a_1 \sim \tilde{a}_1 \nu$, $a_3 \sim \tilde{a}_3 \nu$ and $\delta \sim \tilde{\delta}\nu$, as $\nu \to 0$, for later reference.

First, to understand the emergence of a diode effect, we use $\Gamma(\boldsymbol{q}) - \Gamma(-\boldsymbol{q}) \neq 0$ as a necessary condition for it. Considering the patch theory expansion in Eqs. (5.12) and (5.13), we find

$$\Gamma(\boldsymbol{q}) - \Gamma(-\boldsymbol{q}) = \frac{3}{2}q_x\left(q_x^2 - 3q_y^2\right)(4a_4\delta - a_3). \tag{5.14}$$

This asymmetry vanishes if $\nu = 0$ and no diode effect is possible, in accordance with our symmetry analysis Sec. IV B, as time-reversal (or C_{2z}) symmetry is preserved at $\nu = 0$. Generically, it holds $4\tilde{a}_4\tilde{\delta} \neq \tilde{a}_3$ and we see that the asymmetric part in Eq. (5.14) becomes non-zero immediately when ν is turned on. As such, the diode effect is expected to set in immediately when ν becomes non-zero; this will be confirmed by our explicit model calculations below.

Second, to derive a sufficient condition for finite-$\boldsymbol{q}$ pairing, we expand Eq. (5.12) to quadratic order in $\boldsymbol{q}$, yielding

$$\Gamma(\boldsymbol{q}) \sim \Gamma(\boldsymbol{q} = 0) + \gamma\boldsymbol{q}^2, \quad \boldsymbol{q} \to 0, \tag{5.15a}$$
$$\gamma = -\frac{3}{2}\left[a_2 + c + (6a_4\delta^2 - 3\delta a_3)\right]. \tag{5.15b}$$

Recalling that $a_3 \sim \tilde{a}_3\nu$ and $\delta \sim \tilde{\delta}\nu$, we have $\gamma|_{\nu=0} = -3(a_2 + c)/2 < 0$ (since $\boldsymbol{q} = 0$ pairing must be favored at $\nu = 0$) and there is a critical valley polarization,

$$\nu_c \simeq \sqrt{\frac{a_2 + c}{3(\tilde{a}_3 - 2\tilde{\delta}a_4)\tilde{\delta}}}, \tag{5.16}$$

that $|\nu|$ needs to exceed to turn the maximum at $\boldsymbol{q} = 0$ into a (local) minimum. Note that the value of ν_c

in Eq. (5.16) is technically only an upper bound on the critical valley polarization, as the global minimum can occur at $\boldsymbol{q} \neq 0$ before the maximum at $\boldsymbol{q} = 0$ turns into a local minimum. Nonetheless, the true critical $|\nu|$ must be finite since we expect Γ to depend smoothly on ν. We will revisit this conclusion in our treatment of full MBZ toy models, Sec. V C.

Once $|\nu|$ is larger than this critical value, pairing at finite momentum occurs. Intuitively, this behavior can be understood as follows: the role of valley polarization is to remove the degeneracy between a point at $\boldsymbol{k}$ on the blue Fermi surface and at $-\boldsymbol{k}$ on the red one in Fig. 4(a); this reduces the condensation energy of the superconductor. Choosing a finite $\boldsymbol{q}$ for pairing appropriately can improve the energetics for the superconductor in only two of the three solid segments in Fig. 4(a) [or, equivalently, terms in Eq. (5.12)]. If valley polarization is sufficiently large, the energetic gain by two of the three patches or terms can overcompensate the disfavored one, leading to finite-momentum pairing.

C. Full MBZ toy models

We now extend the discussion from above to include the full MBZ. Our primary focus is to demonstrate the ZFDE, finite $\boldsymbol{q}$ paring and nematicity. To this end, we introduce a toy model to illuminate the role of valley polarization, and for completeness, strain.

We construct a minimal model that captures the symmetries and basic form of the Fermi surfaces of tTLG: for each valley $\eta = \pm$, we consider a nearest-neighbor hopping (t) triangular-lattice model with staggered flux, ϕ_η, that preserves translational and C_{3z} rotational symmetry but breaks time-reversal and C_{2z} in each valley. In order to describe finite strain, $\beta \neq 0$, we replace the hopping along two of the three nearest-neighbor bonds by $t(1 - \beta)$. Explicitly, the dispersions take the form

$$E_{\boldsymbol{k},+} = \epsilon_{\boldsymbol{k};\phi_+} - \mu, \quad E_{\boldsymbol{k},-} = \epsilon_{-\boldsymbol{k};\phi_-} - (\mu + \delta\mu),$$

$$\epsilon_{\boldsymbol{k};\phi} = -t \cos\left(k_x - \frac{\phi}{3}\right)$$

$$- 2t(1 - \beta) \cos\left(\frac{\sqrt{3}k_y}{2}\right) \cos\left(\frac{1}{6}(3k_x + 2\phi)\right). \quad (5.17)$$

Let us start first with the time-reversal, C_{2z}, and C_{3z} symmetric limit by setting $\delta\mu = 0$, $\phi_+ = \phi_-$, and $\beta = 0$. In that case, a state at the Fermi surface at $\boldsymbol{k}$ and one valley η will be degenerate with a state at $-\boldsymbol{k}$ in the other, see Fig. 5(ai). As such, we expect $\Gamma(\boldsymbol{q})$ is peaked at $\boldsymbol{q} = 0$, consistent with Fig. 5(aii), and exhibits the usual logarithmic divergence with temperature. By the same token (C_{2z} or time-reversal symmetry, leading to $E_{\boldsymbol{k},+} = E_{-\boldsymbol{k},-}$), it follows from Eq. (5.4) that $\Gamma(\boldsymbol{q}) = \Gamma(-\boldsymbol{q})$ and there is no diode effect; this can be seen in Fig. 5(aiii).
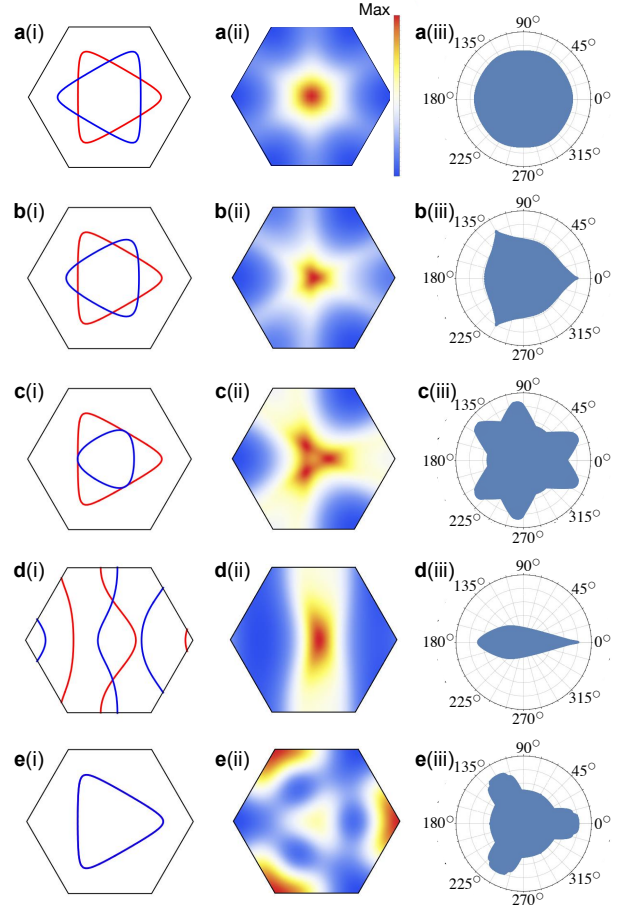

FIG. 5: Diode effect in the minimal model Eq. (5.17). Columns are marked (i), (ii), (iii), which show: (i) the Fermi surfaces of the states undergoing pairing, with valley $\eta = +$ ($\eta = -$) shown in red (blue), (ii) the susceptibility $\Gamma(\boldsymbol{q})$, (iii) the current $J(\hat{n})$ as a function of the direction of $\hat{n} = (\cos\varphi, \sin\varphi)$; the critical current for a given direction $\hat{n}$ is set by the boundary. For Γ and the current, we have set $T = t/10$ and $1/g = \max_{\boldsymbol{q}} \Gamma(\boldsymbol{q})/2$ to evaluate $J(\hat{n})$. Each row represents a qualitatively different scenario arising from the model Eq. (5.17): (a) no valley polarization, no strain, (b) weak valley polarization, no strain, (c) strong valley polarization, no strain (d) (weak) valley polarization, with strain, (e) intravalley pairing, no strain. Explicit parameters are given by [60].

To obtain a diode effect, let us assume C_{2z} and time-reversal symmetry are broken due to finite valley polarization. In our model in Eq. (5.17), we capture this by setting $\delta\mu \neq 0$ or $\phi_+ \neq \phi_-$. It now holds $E_{\boldsymbol{k},+} \neq E_{-\boldsymbol{k},-}$, as is reflected in the Fermi surfaces of, e.g., Fig. 5(bi), and thus $\Gamma(\boldsymbol{q}) \neq \Gamma(-\boldsymbol{q})$ supporting a diode effect, see Fig. 5(bii) and (biii), respectively. Moreover, since C_{3z} is unbroken, the diode effect is seen to be three-fold rotational symmetric, Fig. 5(biii). Note, however, that the maximum of $\Gamma(\boldsymbol{q})$ still occurs at $\boldsymbol{q} = 0$, such that the Cooper pairs still have vanishing center of mass momentum. In fact, this was generically expected since C_{3z}

symmetry implies $\Gamma(\boldsymbol{q}) = \Gamma(C_{3z}\boldsymbol{q})$ and thus the form (5.15a) of the small-$\boldsymbol{q}$ expansion will still hold. We know that $\gamma < 0$ for $\delta\mu = \phi_+ - \phi_- = 0$ and, hence, γ has to remain negative when these two quantities are turned on smoothly. This also agrees with our patch-theory analysis of Sec. V B, where the measure of valley polarization, ν, had to surpass a critical value Eq. (5.16) to induce finite-momentum pairing. Most importantly, this shows that finite-momentum pairing is not only not sufficient for a diode effect (as established above) but also not necessary.

To demonstrate explicitly that the MBZ model can support finite-momentum pairing, we repeat the analysis for larger valley polarization above the critical value (which, as we note in passing, depends on temperature). We indeed find, see Fig. 5(c), that for sufficiently large valley polarization, $\max\Gamma(\boldsymbol{q}) = \Gamma(\boldsymbol{q}_0 \neq \boldsymbol{0})$ which supports finite momentum (i.e. $\boldsymbol{q}_0$) pairing, in agreement with the patch model of Sec. V B.

Once C_{3z} is explicitly broken in the normal state above the superconducting transition, due to finite strain $\beta \neq 0$ or electronic nematic order, we generically expect the critical value of valley polarization for finite-momentum-pairing to vanish: since the constraint $\Gamma(\boldsymbol{q}) = \Gamma(C_{3z}\boldsymbol{q})$ is absent, linear-in-$\boldsymbol{q}$ terms are allowed in the expansion of Γ for small $\boldsymbol{q}$, once C_{2z} and time-reversal are broken by valley polarization. The maximum of $\Gamma(\boldsymbol{q})$ can then immediately occur at a non-zero momentum when valley polarization is introduced. In Fig. 5(d) we present results for a computation with strain β, where we apply quite large β to make the effect and the resulting lack of C_{3z} symmetry in the diode effect clearly visible.

In the limit of sufficiently strong valley polarization, or via other mechanisms, pairing may take place between states within a single valley, thereby breaking TRS and C_{2z}. For completeness, we also consider this *intravalley pairing* scenario within the minimal model Eq. (5.17). We indeed find, in Fig. 5(e), that it generates a ZFDE. It is also seen, from Fig. 5(eii), that $\max\Gamma(\boldsymbol{q}) = \Gamma(\boldsymbol{q}_0 \neq \boldsymbol{0})$; the intravalley state supports pairing at momentum $\boldsymbol{K}_i + \boldsymbol{q}_0$, where $\boldsymbol{q}_0 \in$MBZ and $\boldsymbol{K}_i$ are the BZ (not MBZ) corners. As such, this exotic order parameter exhibits spatial (phase) modulations on the scale of the microscopic graphene layers, producing Kekulé-like patterns, see e.g. [61].

Note that once $\Gamma(\boldsymbol{q})$ is maximal at a non-zero $\boldsymbol{q} = \boldsymbol{q}_0$, as in Fig. 5(cii), the superconductor will spontaneously break the rotational symmetry C_{3z}^s, in gauge-invariant observables. This can be most easily seen by defining the following composite order parameter

$$\mathcal{N}_j = \frac{1}{V}\int d\boldsymbol{x}\,\mathrm{tr}\left[\Delta^\dagger(\boldsymbol{x})(-i\partial_j - 2eA_j)\Delta(\boldsymbol{x})\right], \quad (5.18)$$

$j = x, y$, where the integral is over the volume of the system, $\Delta(\boldsymbol{x})$ is the Fourier transform of the superconducting order parameter $\Delta_{\boldsymbol{q}}$ in Eq. (5.3), and A_j the vector potential. Note that $\mathcal{N}_j$ in Eq. (5.18) is invariant under spin-rotations $\mathrm{SO}(3)_s$ [in fact, even invariant under the full $\mathrm{SU}(2)_+ \times \mathrm{SU}(2)_-$ symmetry], under U(1) gauge transformations, and under $\mathrm{U}(1)_v$, but transforms as the vector (x, y) under C_{3z}. As such, it can couple to physical observables such as the local density of states or the excitation spectrum of the Bogoliubov quasi-particles of the superconductor that will, in turn, exhibit broken C_{3z} symmetry. In addition, by virtue of not breaking any continuous symmetry, $\mathcal{N}_j$ in Eq. (5.18) can have long-range order at finite temperature in two dimensions (via a three-state Potts transition). It is possible that $\mathcal{N}_j$ condenses before the system exhibits significant quasi-long-range order in the superconducting phase. This "vestigial" nematic phase [54] can provide a possible explanation of the observed nematic transport properties above but in the vicinity of the superconducting critical temperature [20]. We note that the critical current $J_c(\hat{n})$ in Fig. 5(ciii) of this nematic state is still C_{3z} symmetric. This is a consequence of the assumption in our calculation that the superconductor will always be able to minimize the free energy of the system (cf. discussion of the $E_{(1,i)}$ in Sec. IV D).

D. Continuum model results

We now work directly with the continuum model for tTLG in Eq. (2.1), both with and without SOC coupling, Eq. (2.2), which arises due to proximity coupling to the WSe$_2$ layer. As above, our primary focus is spontaneous valley polarization as the source of TRS and C_{2z} breaking. To account for valley polarization within the tTLG model, we add to h in Eq. (2.1b) the perturbation $h^V = V_0\sigma_0\eta_z s_0$, which acts simply as a valley-dependent shift of the chemical potential.

To understand the salient features, Fig. 6(a) and (b) present the Fermi surfaces, $\Gamma(\boldsymbol{q})$, and critical current, showing the ZFDE, (a) without SOC and (b) with strong SOC, $\lambda_I = \lambda_R = 10$ meV. In both cases, valley polarization is set to $V_0 = 1$ meV. Inclusion of SOC indeed has an effect on the critical current, compare Fig. 6(a)(iii) and (b)(iii); however, it is seen not to be a necessary ingredient for the ZFDE, in agreement with our toy model calculations of Sec. V C and Table III, showing that VP order will induce a ZFDE without SOC. The results presented in Fig. 6 are obtained using the formalism of Sec. V A. Moreover, the following assumptions are made: First, as discussed in Sec. III, intervalley pairing is likely dominant, and is therefore assumed. Second, the chemical potential is selected to maintain an approximately equal area of the larger Fermi surface for all different parameter sets presented in Fig. 6. Third, noting that the free energy expansion, which leads to expression for $\Gamma(\boldsymbol{q}, T)$ (5.4), is valid for $T \lesssim T_c$, we compute at $T = 0.1$ meV

$\lesssim T_C$; the scale for T_c follows from Ref. 20. Finally, for demonstration, we compute the current assuming an interaction coupling strength $g^{-1} = 0.8 \max_{\boldsymbol{q}} \Gamma(\boldsymbol{q})$.

As discussed in [3–5], having a non-zero Rashba SOC and in-plane field breaks C_{2z}, generates a finite momentum, *helical* pairing state, and is therefore expected to generate a diode effect. Experimentally, it was found, however, that the field-induced diode effect is very weak in the tTLG on WSe$_2$ [20]. To demonstrate that this can be understood as a consequence of the different form of the SOC terms in the tTLG/WSe$_2$ heterostructure, we here consider the case where TRS breaking comes from an applied in-plane magnetic field, instead of valley polarization. To account for the in-plane field, we add to (2.1b) the Zeeman coupling $h^B = \sigma_0 \eta_0 \boldsymbol{B}_\parallel \cdot \boldsymbol{s}$. It has a more subtle impact on the bandstructure than valley polarization, which also crucially depends on λ_R, λ_I.

Fig. 6(c) and (d) present results for tTLG with SOC and a large in-plane Zeeman field, $\boldsymbol{B}_\parallel = B\hat{x}$, with $B = 10$ T. To demonstrate that, in accordance with our symmetry-analysis in Sec. IV C, Rashba SOC is a necessary perturbation for the in-plane Zeeman-field diode mechanism, we consider two limits: In Fig. 6(c) a moderate Rashba coupling $\lambda_R = 1$ meV, while in Fig. 6(d), a large Rashba coupling $\lambda_R = 10$ meV are assumed. In both cases we fix $\lambda_I = 10$ meV, which is motivated by the analysis in Ref. 35. Comparison of Fig. 6(d)(iii) and (e)(iii) demonstrates the role played by Rashba SOC, and further that Ising SOC alone is insufficient to generate a diode effect. In particular, the diode effect in Fig. 6(ciii) is rather weak, despite the large magnetic field. This might explain why the untrained sample with ZFDE of Ref. 20 does not show any significant $\delta J_c(\hat{n})$ when in-plane fields are applied.

VI. DOPING DEPENDENCE OF THE DIODE EFFECT

One particularly striking observation of Ref. 20 is that the sign of the diode effect, i.e., the sign of $\delta J_c(\hat{n})$ in Eq. (4.2) for fixed direction $\hat{n}$, changes once the filling fraction ν_{tTLG} is tuned from electron, $\nu_{\text{tTLG}} > 0$, to hole, $\nu_{\text{tTLG}} < 0$, doping or vice versa. In this section, we will present a theoretical explanation for why this behavior might be expected and discuss implications for the doping dependence of the order parameter of the normal-state instability inducing the diode effect.

As argued in Sec. IV B, the diode effect can be induced by one of the six normal-state orders in Table III. The magnetic-field training behavior in experiment [20] points towards one of the first four states, SP$_\perp$, VP, SSLP$_\perp^+$ or SLP$^-$, which start to mix once both λ_I and λ_R are non-zero. Therefore, to keep the discussion simple, we will focus on VP here and first neglect SOC altogether.
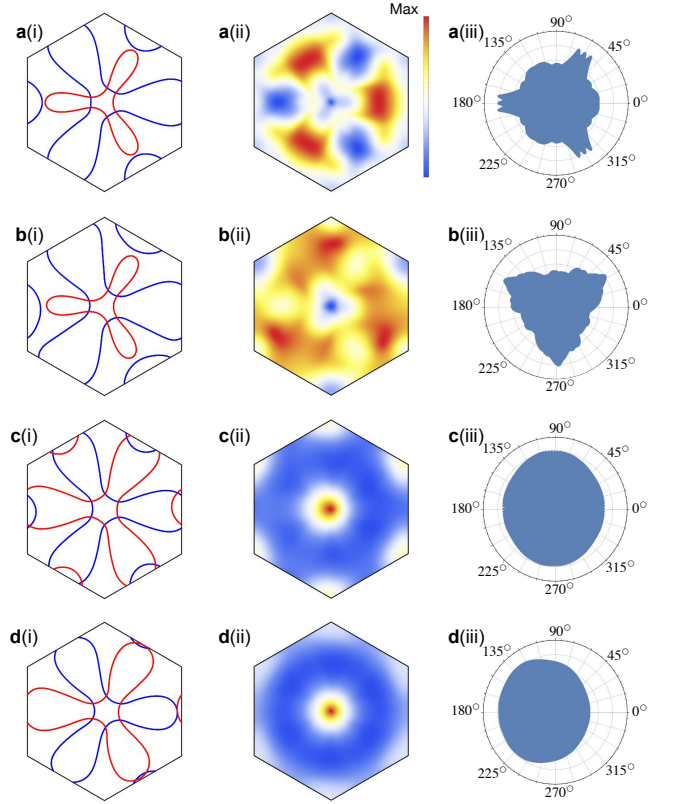

FIG. 6: Diode effect in the tTLG model Eq. (2.1). Columns are marked (i), (ii), (iii), which show: (i) the Fermi surfaces of the states undergoing pairing, with valley $\eta = +$ ($\eta = -$) shown in red (blue), (ii) the susceptibility $\Gamma(\boldsymbol{q})$, (iii) the current $J(\hat{n})$ as a function of the direction of $\hat{n} = (\cos\varphi, \sin\varphi)$; the critical current for a given direction $\hat{n}$ is set by the boundary. Row (a) tTLG, no SOC, $\mu = 8.5$ meV, and valley polarization $V_0 = 1$ meV, (b) tTLG + WSe$_2$ with SOC $\lambda_R = \lambda_I = 10$ meV, $\mu = 12.3$ meV, and valley polarization $V_0 = 1$ meV. (c) tTLG + WSe$_2$, $\lambda_R = 1$, $\lambda_I = 10$ meV, $\mu = 12.7$ meV, and an in-plane field $B_x = 10$ T, (d) tTLG + WSe$_2$, $\lambda_R = \lambda_I = 10$ meV, $\mu = 12.7$ meV, and an in-plane field $B_x = 10$ T. Everywhere, $T = 0.1$ meV and $\theta = 1.5$ degrees.

An effective mean-field model for electron doping, $\nu_{\text{tTLG}} > 0$, in the presence of VP then reads as

$$H_{\text{eff}}^{\text{LE}} = \sum_{\boldsymbol{k}} f_{\boldsymbol{k},\eta,s}^\dagger E_{\boldsymbol{k},\eta} f_{\boldsymbol{k},\eta,s}, \ E_{\boldsymbol{k},\pm} = \xi_{\pm\boldsymbol{k}} + V_z g_{\boldsymbol{k},\pm}, \ (6.1)$$

where $f_{\boldsymbol{k},\eta,s}^\dagger$ ($f_{\boldsymbol{k},\eta,s}$) are the creation (annihilation) operators, already introduced in Eq. (2.3), for electrons with spin quantum number s, in valley η, in the band that is closest to the Fermi level at momentum $\boldsymbol{k}$. As in Eq. (2.4), $\xi_{\boldsymbol{k}}$ parametrizes the associated bandstructure in the absence of VP, $V_z = 0$, and $g_{\boldsymbol{k},\eta}$ is the form factor of the valley order; we will not further have to specify $g_{\boldsymbol{k},\eta}$ and only use that it has to be odd under time-reversal

and, thus, obey

$$g_{\boldsymbol{k},\eta} = -g_{-\boldsymbol{k},-\eta}, \quad \eta = \pm, \, \forall \, \boldsymbol{k}. \qquad (6.2)$$

To establish a relation between the bandstructure for electron and hole doping, let us denote the twisted-bilayer-graphene-like flat bands [48] above ($p = +$) and below ($p = -$) the charge neutrality point in valley η by $\epsilon_{\boldsymbol{k},p,\eta}$. As shown in [48], a finite displacement field strongly violates the "particle-hole-like" symmetry $\epsilon_{\boldsymbol{k},p,\eta} = -\epsilon_{-\boldsymbol{k},-p,\eta}$ in tTLG (in contrast to the continuum model of twisted-bilayer graphene where it becomes exact in the limit of small twist angles). Instead, the "chiral symmetry",

$$\epsilon_{\boldsymbol{k},p,\eta} = -\epsilon_{\boldsymbol{k},-p,\eta}, \qquad (6.3)$$

turns out to be approximately obeyed for realistic parameters [becomes exact in the limit where the interlayer tunneling between same sublattices, w_0 in h^{t} in Eq. (2.1b), is set to zero].

If we *assume* that both the strength and sign of the VP V_z and the functional form of $g_{\boldsymbol{k},\pm}$ are invariant under $\nu_{\mathrm{tTLG}} \to -\nu_{\mathrm{tTLG}}$, we conclude from Eq. (6.3) that the effective model for the hole-doped region is given by Eq. (6.1) with

$$E_{\boldsymbol{k},\pm} \longrightarrow \bar{E}_{\boldsymbol{k},\pm} = -\xi_{\pm\boldsymbol{k}} + V_z g_{\boldsymbol{k},\pm} = -E_{-\boldsymbol{k},\mp}, \quad (6.4)$$

where we have used Eq. (6.2) in the last equality. Inspection of Eq. (5.4) yields that $\Gamma(\boldsymbol{q})$ for electrons (Γ^e) and for holes (Γ^h) are, thus, related by

$$\Gamma^e(\boldsymbol{q}) = \Gamma^h(-\boldsymbol{q}). \qquad (6.5)$$

From Eq. (5.7), we immediately get the relation $\boldsymbol{J}^e(\boldsymbol{q}) = -\boldsymbol{J}^h(-\boldsymbol{q})$ and thus $J_c^e(\hat{n}) = J_c^h(-\hat{n})$; this, in turn, directly implies

$$\delta J_c^e(\hat{n}) = -\delta J_c^h(\hat{n}). \qquad (6.6)$$

This shows that the sign reversal of the diode effect between electron and hole doping can be readily understood from the approximate chiral symmetry, Eq. (6.3), of the bandstructure. Within this picture, it also follows that the sign of the order parameter, V_z, of valley-polarization does not change in experiment [20] when sweeping ν_{tTLG} between electron and hole doping. The mechanism fixing the effective sign of V_z when changing the electron density at zero external field might be related to the interpretation of recent observations on twisted monolayer-bilayer graphene [62, 63].

Of course, in the realistic system neither Eq. (6.3) is obeyed exactly nor will V_z and $g_{\boldsymbol{k},\pm}$ be exactly the same for particle and hole doping (and SOC represents another perturbation), which would explain the reason why the measured magnitude of $\delta J_c^e(\hat{n})$ and $\delta J_c^h(\hat{n})$ are not exactly the same [20].

VII. CONCLUSION AND OUTLOOK

We presented a microscopic theory, and detailed analysis of the necessary conditions, for the ZFDE observed [20] in the tTLG-WSe$_2$ heterostructure in Fig. 1. We use a combination of general symmetry arguments and explicit model computations, determine the possible superconducting (summarized in Fig. 2) and normal-state instabilities (see summary in Fig. 3 and Table II) of the system, study the emergence of vestigial orders [cf. Eqs. (4.3) and (5.18)], and the influence of SOC and external magnetic fields on the ZFDE. Taken together, our results offer an explanation of several key findings reported in [20]—in particular, the field trainability and doping dependence of the ZFDE, as well as the enhanced transverse resistance above the superconducting transition.

We discussed two different microscopic origins of the ZFDE: either (a) time-reversal symmetry is preserved in the normal state but broken spontaneously by the superconducting phase (see Sec. IV D) or (b) it is already broken in the normal state as a result of one of the candidate particle-hole instabilities summarized in Table II. In case of the latter, we showed that only the states listed in Table III can yield a ZFDE, where the first four (last two) states become symmetry-equivalent in the presence of strong SOC. We also derived the field trainability of these candidate states, showing that the first set of four states in Table III is more consistent with experiment [20]. Motivated by the fact that all of these states exhibit valley polarization in the presence of SOC, it would be interesting to explicitly control valley polarization in future experiments through the use of combined strain-induced artificial magnetic fields and real magnetic fields, as demonstrated in single-layer graphene [64].

Invoking the approximate chiral symmetry of the system, we have provided in Sec. VI an explanation of the observed sign change of the current asymmetry δJ_c in Eq. (4.2) with doping—from electron to hole filling. Since moiré systems host ultralow carrier density and narrow bandwidths, electrostatic gating is able to *in situ* control the doping and therefore the diode effect. Hence, the ZFDE in moiré systems is both generated and manipulated without recourse to external magnetic fields, and thereby offers an interesting platform for future technological applications.

We considered composite order parameters, defined in Eqs. (4.3) and (5.18), that capture, respectively, the broken time-reversal and rotational symmetry of the superconducting phases in scenario (a) and (b) above. Moreover, their condensation above the resistive superconducting transition defines vestigial phases that provide an appealing interpretation for the enhanced transverse resistance measurements in the vicinity of the critical temperature $T \gtrsim T_c$ [20]. Relatedly, considering the region $T \gtrsim T_c$ there have been earlier works reporting non-

reciprocal paraconductivity for Rashba superconductors in a magnetic field [65–67]. It would be interesting to extend the theory presented here to include superconducting fluctuations to examine the possibility of zero-field, paraconducting, non-reciprocal charge transport.

We point out an *extreme* diode effect was observed for certain electron fillings in [20], whereby a current is needed to stabilize superconductivity. Within our theory, this might be most naturally understood by noting that the underlying magnetic order inducing the ZFDE also weakens superconductivity at the same time; if an applied current acts to weaken the magnetic order, this will, in turn, promote superconductivity that was previously destabilized by the magnetic order parameter. For the case of valley polarization, this is certainly plausible since current switching of valley polarization in twisted bilayer graphene was demonstrated recently [58, 68, 69].

The interplay of topology and the phenomena considered here is worthy of further investigation, as both inter- and intra-valley pairing in related systems have been shown to host first and higher-order topology [70, 71],

including in the presence of spin-orbit coupling [72]. Furthermore, depending on the precise form of the Fermi surfaces in the magnetically ordered phase of the system, it would also be interesting to generalize the analysis to multiple-q superconducting order parameters.

Our results straightforwardly apply to other twisted graphene systems, yet in light of the recent observation of spin-polarized superconductivity in rhombohedral trilayer graphene [73], it would be interesting to extend our analysis to establish the conditions for zero-field diode effect in that system.

[1] A. Kitai, *Principles of Solar Cells, LEDs and Diodes: The role of the PN junction* (John Wiley & Sons, 2011).

[2] F. Ando, Y. Miyasaka, T. Li, J. Ishizuka, T. Arakawa, Y. Shiota, T. Moriyama, Y. Yanase, and T. Ono, "Observation of superconducting diode effect," Nature **584**, 373 (2020).

[3] A. Daido, Y. Ikeda, and Y. Yanase, "Intrinsic Superconducting Diode Effect," arXiv e-prints (2021), arXiv:2106.03326 [cond-mat.supr-con].

[4] N. F. Q. Yuan and L. Fu, "Supercurrent diode effect and finite momentum superconductivity," arXiv e-prints (2021), arXiv:2106.01909 [cond-mat.supr-con].

[5] J. J. He, Y. Tanaka, and N. Nagaosa, "A Phenomenological Theory of Superconductor Diodes in Presence of Magnetochiral Anisotropy," arXiv e-prints (2021), arXiv:2106.03575 [cond-mat.supr-con].

[6] Y.-Y. Lyu, J. Jiang, Y.-L. Wang, Z.-L. Xiao, S. Dong, Q.-H. Chen, M. V. Milošević, H. Wang, R. Divan, J. E. Pearson, P. Wu, F. M. Peeters, and W.-K. Kwok, "Superconducting diode effect via conformal-mapped nanoholes," Nature Communications **12**, 2703 (2021).

[7] L. Bauriedl, C. Bäuml, L. Fuchs, C. Baumgartner, N. Paulik, J. M. Bauer, K.-Q. Lin, J. M. Lupton, T. Taniguchi, K. Watanabe, C. Strunk, and N. Paradiso, "Supercurrent diode effect and magnetochiral anisotropy in few-layer NbSe$_2$ nanowires," (2021), arXiv:2110.15752 [cond-mat.supr-con].

[8] S. Ilić and F. S. Bergeret, "Effect of disorder on superconducting diodes," arXiv e-prints (2021), arXiv:2108.00209 [cond-mat.supr-con].

[9] J. Shin, S. Son, J. Yun, G. Park, K. Zhang, Y. J. Shin, J.-G. Park, and D. Kim, "Magnetic proximity-induced superconducting diode effect and infinite magnetoresistance in van der waals heterostructure," (2021),

arXiv:2111.05627 [cond-mat.supr-con].

[10] J. Hu, C. Wu, and X. Dai, "Proposed design of a josephson diode," Phys. Rev. Lett. **99**, 067004 (2007).

[11] A. Buzdin, "Direct coupling between magnetism and superconducting current in the josephson φ_0 junction," Phys. Rev. Lett. **101**, 107005 (2008).

[12] D. B. Szombati, S. Nadj-Perge, D. Car, S. R. Plissard, E. P. A. M. Bakkers, and L. P. Kouwenhoven, "Josephson ϕ_0-junction in nanowire quantum dots," Nature Physics **12**, 568 (2016).

[13] A. A. Kopasov, A. G. Kutlin, and A. S. Mel'nikov, "Geometry controlled superconducting diode and anomalous josephson effect triggered by the topological phase transition in curved proximitized nanowires," Phys. Rev. B **103**, 144520 (2021).

[14] C. Baumgartner, L. Fuchs, A. Costa, S. Reinhardt, S. Gronin, G. C. Gardner, T. Lindemann, M. J. Manfra, P. E. Faria Junior, D. Kochan, J. Fabian, N. Paradiso, and C. Strunk, "Supercurrent rectification and magnetochiral effects in symmetric josephson junctions," Nature Nanotechnology (2021), 10.1038/s41565-021-01009-9.

[15] J. Diez-Merida, A. Diez-Carlon, S. Yang, Y.-M. Xie, X.-J. Gao, K. Watanabe, T. Taniguchi, X. Lu, K. Law, and D. K. Efetov, "Magnetic josephson junctions and superconducting diodes in magic angle twisted bilayer graphene," arXiv preprint arXiv:2110.01067 (2021).

[16] C. Baumgartner, L. Fuchs, A. Costa, J. P. Cortes, S. Reinhardt, S. Gronin, G. C. Gardner, T. Lindemann, M. J. Manfra, P. E. F. Junior, D. Kochan, J. Fabian, N. Paradiso, and C. Strunk, "Effect of rashba and dresselhaus spin-orbit coupling on supercurrent rectification and magnetochiral anisotropy of ballistic josephson junctions," (2021), arXiv:2111.13983 [cond-mat.supr-con].

[17] H. Wu, Y. Wang, P. K. Sivakumar, C. Pasco, S. S. P. Parkin, Y.-J. Zeng, T. McQueen, and M. N. Ali, "Realization of the field-free josephson diode," (2021), arXiv:2103.15809 [cond-mat.supr-con].

[18] E. Strambini, M. Spies, N. Ligato, S. Ilic, M. Rouco, C. G. Orellana, M. Ilyn, C. Rogero, F. S. Bergeret, J. S. Moodera, P. Virtanen, T. T. Heikkilä, and F. Giazotto, "Rectification in a eu-chalcogenide-based superconducting diode," (2021), arXiv:2109.01061 [cond-mat.supr-con].

[19] K. Halterman, M. Alidoust, R. Smith, and S. Starr, "Supercurrent Diode Effect, Spin Torques, and Robust Zero-Energy Peak in Planar Half-Metallic Trilayers," arXiv e-prints (2021), arXiv:2111.01242 [cond-mat.supr-con].

[20] J.-X. Lin, P. Siriviboon, H. D. Scammell, S. Liu, D. Rhodes, K. Watanabe, T. Taniguchi, J. Hone, M. S. Scheurer, and J. Li, "Zero-field superconducting diode effect in twisted trilayer graphene," arXiv e-prints (2021), arXiv:2112.07841 [cond-mat.str-el].

[21] J. M. Park, Y. Cao, K. Watanabe, T. Taniguchi, and P. Jarillo-Herrero, "Tunable strongly coupled superconductivity in magic-angle twisted trilayer graphene," Nature 590, 249–255 (2021).

[22] Z. Hao, A. M. Zimmerman, P. Ledwith, E. Khalaf, D. H. Najafabadi, K. Watanabe, T. Taniguchi, A. Vishwanath, and P. Kim, "Electric field–tunable superconductivity in alternating-twist magic-angle trilayer graphene," Science 371, 1133–1138 (2021).

[23] Y. Cao, J. M. Park, K. Watanabe, T. Taniguchi, and P. Jarillo-Herrero, "Large Pauli Limit Violation and Reentrant Superconductivity in Magic-Angle Twisted Trilayer Graphene," arXiv e-prints , arXiv:2103.12083 (2021), arXiv:2103.12083 [cond-mat.mes-hall].

[24] H. Kim, Y. Choi, C. Lewandowski, A. Thomson, Y. Zhang, R. Polski, K. Watanabe, T. Taniguchi, J. Alicea, and S. Nadj-Perge, "Spectroscopic Signatures of Strong Correlations and Unconventional Superconductivity in Twisted Trilayer Graphene," arXiv e-prints (2021), arXiv:2109.12127 [cond-mat.mes-hall].

[25] S. Turkel, J. Swann, Z. Zhu, M. Christos, K. Watanabe, T. Taniguchi, S. Sachdev, M. S. Scheurer, E. Kaxiras, C. R. Dean, and A. N. Pasupathy, "Orderly disorder in magic-angle twisted trilayer graphene," Science 376, 193 (2022).

[26] X. Liu, N. J. Zhang, K. Watanabe, T. Taniguchi, and J. I. A. Li, "Coulomb screening and thermodynamic measurements in magic-angle twisted trilayer graphene," arXiv e-prints (2021), arXiv:2108.03338 [cond-mat.mes-hall].

[27] J. M. B. L. Dos Santos, N. M. R. Peres, and A. H. C. Neto, "Graphene bilayer with a twist: electronic structure," Phys. Rev. Lett. 99, 256802 (2007).

[28] R. Bistritzer and A. H. MacDonald, "Moiré bands in twisted double-layer graphene," Proc. Natl. Acad. Sci. U.S.A. 108, 12233 (2011).

[29] J. M. B. L. Dos Santos, N. M. R. Peres, and A. H. C. Neto, "Continuum model of the twisted graphene bilayer," Phys. Rev. B 86, 155449 (2012).

[30] M. Gmitra and J. Fabian, "Graphene on transition-metal dichalcogenides: A platform for proximity spin-orbit physics and optospintronics," Phys. Rev. B 92, 155403 (2015).

[31] T. Naimer, K. Zollner, M. Gmitra, and J. Fabian, "Twist-angle dependent proximity induced spin-orbit coupling in graphene/transition-metal dichalcogenide heterostructures," arXiv e-prints (2021), arXiv:2108.06126 [cond-mat.mes-hall].

[32] E. Khalaf, A. J. Kruchkov, G. Tarnopolsky, and A. Vishwanath, "Magic angle hierarchy in twisted graphene multilayers," Phys. Rev. B 100, 085109 (2019).

[33] S. Carr, C. Li, Z. Zhu, E. Kaxiras, S. Sachdev, and A. Kruchkov, "Ultraheavy and ultrarelativistic dirac quasiparticles in sandwiched graphenes," Nano Letters 20, 3030 (2020).

[34] C. Mora, N. Regnault, and B. A. Bernevig, "Flatbands and perfect metal in trilayer moiré graphene," Phys. Rev. Lett. 123, 026402 (2019).

[35] P. Siriviboon, J.-X. Lin, H. D. Scammell, S. Liu, D. Rhodes, K. Watanabe, T. Taniguchi, J. Hone, M. S. Scheurer, and J. I. A. Li, "Abundance of density wave phases in twisted trilayer graphene on WSe$_2$," arXiv e-prints (2021), arXiv:2112.07127 [cond-mat.mes-hall].

[36] M. Christos, S. Sachdev, and M. S. Scheurer, "Superconductivity, correlated insulators, and Wess–Zumino–Witten terms in twisted bilayer graphene," Proc. Natl. Acad. Sci. U.S.A. 117, 29543 (2020).

[37] D. Călugăru, F. Xie, Z.-D. Song, B. Lian, N. Regnault, and B. A. Bernevig, "Twisted symmetric trilayer graphene: Single-particle and many-body Hamiltonians and hidden nonlocal symmetries of trilayer moiré systems with and without displacement field," Phys. Rev. B 103, 195411 (2021), arXiv:2102.06201 [cond-mat.str-el].

[38] E. Khalaf, A. J. Kruchkov, G. Tarnopolsky, and A. Vishwanath, "Magic angle hierarchy in twisted graphene multilayers," Physical Review B 100 (2019), 10.1103/physrevb.100.085109.

[39] L. Huder, A. Artaud, T. Le Quang, G. T. de Laissardière, A. G. M. Jansen, G. Lapertot, C. Chapelier, and V. T. Renard, "Electronic spectrum of twisted graphene layers under heterostrain," Phys. Rev. Lett. 120, 156405 (2018).

[40] N. P. Kazmierczak, M. Van Winkle, C. Ophus, K. C. Bustillo, S. Carr, H. G. Brown, J. Ciston, T. Taniguchi, K. Watanabe, and D. K. Bediako, "Strain fields in twisted bilayer graphene," Nature Materials 20, 956 (2021).

[41] A. Kerelsky, L. J. McGilly, D. M. Kennes, L. Xian, M. Yankowitz, S. Chen, K. Watanabe, T. Taniguchi, J. Hone, C. Dean, A. Rubio, and A. N. Pasupathy, "Maximized electron interactions at the magic angle in twisted bilayer graphene," Nature 572, 95 (2019).

[42] Y. Jiang, X. Lai, K. Watanabe, T. Taniguchi, K. Haule, J. Mao, and E. Y. Andrei, "Charge order and broken rotational symmetry in magic-angle twisted bilayer graphene," Nature 573, 91 (2019).

[43] Y. Choi, J. Kemmer, Y. Peng, A. Thomson, H. Arora, R. Polski, Y. Zhang, H. Ren, J. Alicea, G. Refael, F. von Oppen, K. Watanabe, T. Taniguchi, and S. Nadj-Perge, "Electronic correlations in twisted bilayer graphene near the magic angle," Nature Physics 15, 1174 (2019).

[44] Y. Cao, D. Rodan-Legrain, J. M. Park, N. F. Q. Yuan, K. Watanabe, T. Taniguchi, R. M. Fernandes, L. Fu, and P. Jarillo-Herrero, "Nematicity and competing orders

in superconducting magic-angle graphene," Science **372**, 264 (2021).

[45] C. Rubio-Verdú, S. Turkel, Y. Song, L. Klebl, R. Samajdar, M. S. Scheurer, J. W. F. Venderbos, K. Watanabe, T. Taniguchi, H. Ochoa, L. Xian, D. M. Kennes, R. M. Fernandes, Á. Rubio, and A. N. Pasupathy, "Moirénematic phase in twisted double bilayer graphene," Nature Physics **18**, 196 (2022).

[46] Z. Bi, N. F. Q. Yuan, and L. Fu, "Designing flat bands by strain," Phys. Rev. B **100**, 035448 (2019).

[47] R. Samajdar, M. Scheurer, S. Turkel, C. Rubio-Verdú, A. Pasupathy, J. Venderbos, and R. M. Fernandes, "Electric-field-tunable electronic nematic order in twisted double-bilayer graphene," 2D Materials **8** (2021).

[48] M. Christos, S. Sachdev, and M. S. Scheurer, "Correlated insulators, semimetals, and superconductivity in twisted trilayer graphene," Phys. Rev. X **12**, 021018 (2022).

[49] J. Gonzalez and T. Stauber, "*p*-wave superconductivity induced from valley symmetry breaking in twisted trilayer graphene," arXiv e-prints (2021), arXiv:2110.11294 [cond-mat.supr-con].

[50] M. S. Scheurer and R. Samajdar, "Pairing in graphene-based moiré superlattices," Phys. Rev. Research **2**, 033062 (2020).

[51] M. S. Scheurer, "Mechanism, time-reversal symmetry, and topology of superconductivity in noncentrosymmetric systems," Phys. Rev. B **93**, 174509 (2016).

[52] R. Samajdar and M. S. Scheurer, "Microscopic pairing mechanism, order parameter, and disorder sensitivity in moiré superlattices: Applications to twisted double-bilayer graphene," Phys. Rev. B **102**, 064501 (2020).

[53] M. S. Scheurer, D. F. Agterberg, and J. Schmalian, "Selection rules for cooper pairing in two-dimensional interfaces and sheets," npj Quantum Materials **2**, 9 (2017).

[54] R. M. Fernandes, P. P. Orth, and J. Schmalian, "Intertwined vestigial order in quantum materials: Nematicity and beyond," Annual Review of Condensed Matter Physics **10**, 133 (2019).

[55] B. Zinkl, K. Hamamoto, and M. Sigrist, "Symmetry conditions for the superconducting diode effect in chiral superconductors," (2021), arXiv:2111.05340 [cond-mat.supr-con].

[56] J. Hooper, Z. Q. Mao, K. D. Nelson, Y. Liu, M. Wada, and Y. Maeno, "Anomalous josephson network in the Ru-sr$_2$ruo$_4$ eutectic system," Phys. Rev. B **70**, 014510 (2004).

[57] J. Liu and X. Dai, "Orbital magnetic states in moiré graphene systems," Nature Reviews Physics **3**, 367 (2021).

[58] A. L. Sharpe, E. J. Fox, A. W. Barnard, J. Finney, K. Watanabe, T. Taniguchi, M. A. Kastner, and D. Goldhaber-Gordon, "Emergent ferromagnetism near three-quarters filling in twisted bilayer graphene," Science **365**, 605 (2019).

[59] J.-X. Lin, Y.-H. Zhang, E. Morissette, Z. Wang, S. Liu, D. Rhodes, K. Watanabe, T. Taniguchi, J. Hone, and J. I. A. Li, "Spin-orbit driven ferromagnetism at half moiré filling in magic-angle twisted bilayer graphene," arXiv e-prints (2021), arXiv:2102.06566 [cond-mat.mes-hall].

[60] (a) without strain or valley polarization $\mu/t = -0.68; \phi_+ = \phi_- = -0.7\pi; \delta\mu = \beta = 0$, (b) with *weak* valley polarization but without strain ($\mu/t = -0.68; \phi_+ = \phi_= - 0.7\pi; \delta\mu/t = -0.2; \beta = 0$), (c) with *strong* valley polarization but without strain ($\mu/t = -0.68; \phi_+ = \phi_= - 0.7\pi; \delta\mu/t = -0.6; \beta = 0$), (d) *weak* valley polarization in the presence of strain ($\mu/t = -0.42; \phi_+ = -0.8\pi, \phi_- = -1.1\pi; \delta\mu/t = -0.1; \beta = 0.5$), (e) intravalley pairing, no strain ($\mu/t = -0.68; \phi_+ = \phi_- = -0.7\pi; \beta = 0$).

[61] B. Roy and I. F. Herbut, "Unconventional superconductivity on honeycomb lattice: Theory of kekule order parameter," Phys. Rev. B **82**, 035429 (2010).

[62] H. Polshyn, J. Zhu, M. A. Kumar, Y. Zhang, F. Yang, C. L. Tschirhart, M. Serlin, K. Watanabe, T. Taniguchi, A. H. MacDonald, and A. F. Young, "Electrical switching of magnetic order in an orbital chern insulator," Nature **588**, 66 (2020).

[63] J. Zhu, J.-J. Su, and A. H. MacDonald, "Voltage-controlled magnetic reversal in orbital chern insulators," Phys. Rev. Lett. **125**, 227702 (2020).

[64] S.-Y. Li, Y. Su, Y.-N. Ren, and L. He, "Valley polarization and inversion in strained graphene via pseudo-landau levels, valley splitting of real landau levels, and confined states," Phys. Rev. Lett. **124**, 106802 (2020).

[65] R. Wakatsuki, Y. Saito, S. Hoshino, Y. M. Itahashi, T. Ideue, M. Ezawa, Y. Iwasa, and N. Nagaosa, "Nonreciprocal charge transport in noncentrosymmetric superconductors," Science Advances **3**, e1602390 (2017).

[66] R. Wakatsuki and N. Nagaosa, "Nonreciprocal current in noncentrosymmetric rashba superconductors," Phys. Rev. Lett. **121**, 026601 (2018).

[67] S. Hoshino, R. Wakatsuki, K. Hamamoto, and N. Nagaosa, "Nonreciprocal charge transport in two-dimensional noncentrosymmetric superconductors," Phys. Rev. B **98**, 054510 (2018).

[68] M. Serlin, C. L. Tschirhart, H. Polshyn, Y. Zhang, J. Zhu, K. Watanabe, T. Taniguchi, L. Balents, and A. F. Young, "Intrinsic quantized anomalous hall effect in a moire heterostructure," Science **367**, 900 (2020).

[69] X. Ying, M. Ye, and L. Balents, "Current switching of valley polarization in twisted bilayer graphene," Phys. Rev. B **103**, 115436 (2021).

[70] A. Chew, Y. Wang, B. A. Bernevig, and Z.-D. Song, "Higher-order topological superconductivity in twisted bilayer graphene," (2021), arXiv:2108.05373 [cond-mat.supr-con].

[71] T. Li, M. Geier, J. Ingham, and H. Scammell, "Higher-order topological superconductivity from repulsive interactions in kagome and honeycomb systems," 2D Materials (2021).

[72] H. D. Scammell, J. Ingham, M. Geier, and T. Li, "Intrinsic first and higher-order topological superconductivity in a doped topological insulator," (2021), arXiv:2111.07252 [cond-mat.supr-con].

[73] H. Zhou, T. Xie, T. Taniguchi, K. Watanabe, and A. F. Young, "Superconductivity in rhombohedral trilayer graphene," Nature **598**, 434 (2021).

Appendix A: Continuum model

The continuum Hamiltonian is described in detail in Section II A. For clarity, here we additionally provide the explicit momentum space representation.

To establish the Hamiltonian in momentum space, we denote by $c_{\boldsymbol{k};\rho,l,\eta,s,\boldsymbol{G}}$ the electron annihilation operator with the following quantum numbers: crystalline momentum $\boldsymbol{k}$ within the moiré Brillouin zone (MBZ); spin $s = \uparrow, \downarrow$; sublattice $\rho = A, B$; valley $\eta = \pm$ of the graphene layer $\ell = 1, 2, 3$; and reciprocal lattice (RL) vector $\boldsymbol{G} = \sum_{j=1,2} n_j \boldsymbol{G}_j$, $n_j \in \mathbb{Z}$ of the effective moiré lattice.

The unitary transformation in layer space,

$$c_{\boldsymbol{k};\rho,l,\eta,s,\boldsymbol{G}} = V_{l,\ell}\psi_{\boldsymbol{k};\rho,\ell,\eta,s,\boldsymbol{G}}, \qquad V = \frac{1}{\sqrt{2}}\begin{pmatrix} 1 & 0 & -1 \\ 0 & \sqrt{2} & 0 \\ 1 & 0 & 1 \end{pmatrix}, \tag{A1}$$

conveniently decomposes the system into mirror-even ($\ell = 1, 2$) and mirror-odd ($\ell = 3$) subspaces, which become mixed at nonzero D_0 or SOC. Working in this mirror basis, the full continuum model described in the main text is

$$H_0 = \sum_{\boldsymbol{k}\in\mathrm{MBZ}} \sum_{\rho,\rho'=A,B} \sum_{\ell,\ell'=1,2,3} \sum_{\eta=\pm} \sum_{s=\uparrow,\downarrow} \sum_{\boldsymbol{G},\boldsymbol{G}'\in\mathrm{RL}} \psi^\dagger_{\boldsymbol{k};\rho,\ell,\eta,s,\boldsymbol{G}} \left(h_{\boldsymbol{k},\eta}\right)_{\rho,\ell,\boldsymbol{G};\rho',\ell',\boldsymbol{G}'} \psi_{\boldsymbol{k};\rho',\ell',\eta,s,\boldsymbol{G}'},$$
$$h_{\boldsymbol{k},\eta} = h^{(g)}_{\boldsymbol{k},\eta} + h^{(t)}_{\boldsymbol{k},\eta} + h^{(D)}_{\boldsymbol{k}} + h^{(\mathrm{SOC})}_{\boldsymbol{k},\eta}. \tag{A2}$$

The corresponding components are given by,

$$\left(h^{(g)}_{\boldsymbol{k},+}\right)_{\rho,\ell,\boldsymbol{G};\rho',\ell',\boldsymbol{G}'} = \delta_{\ell,\ell'}\delta_{\boldsymbol{G},\boldsymbol{G}'} v_F (\boldsymbol{\rho}_{\theta_\ell})_{\rho,\rho'} \left(\boldsymbol{k} + \boldsymbol{G} - (-1)^\ell \boldsymbol{q}_1/2\right), \tag{A3a}$$

$$\left(h^{(g)}_{\boldsymbol{k},-}\right)_{\rho,\ell,\boldsymbol{G};\rho',\ell',\boldsymbol{G}'} = \left(h^{(g)}_{-\boldsymbol{k},+}\right)^*_{\rho,\ell,-\boldsymbol{G};\rho',\ell',-\boldsymbol{G}'}, \tag{A3b}$$

$$\left(h^{(t)}_{\boldsymbol{k},+}\right)_{\rho,\ell,\boldsymbol{G};\rho',\ell',\boldsymbol{G}'} = \sqrt{2}\begin{pmatrix} 0 & (T_{\boldsymbol{G}-\boldsymbol{G}'})_{\rho,\rho'} & 0 \\ (T^*_{\boldsymbol{G}'-\boldsymbol{G}})_{\rho',\rho} & 0 & 0 \\ 0 & 0 & 0 \end{pmatrix}_{\ell,\ell'}, \tag{A3c}$$

$$\left(h^{(t)}_{\boldsymbol{k},-}\right)_{\rho,\ell,\boldsymbol{G};\rho',\ell',\boldsymbol{G}'} = \left(h^{(t)}_{-\boldsymbol{k},+}\right)^*_{\rho,\ell,-\boldsymbol{G};\rho',\ell',-\boldsymbol{G}'}, \tag{A3d}$$

$$\left(h^{(D)}_{\boldsymbol{k}}\right)_{\rho,\ell,\boldsymbol{G};\rho',\ell',\boldsymbol{G}'} = -D_0\delta_{\rho,\rho'}\delta_{\boldsymbol{G},\boldsymbol{G}'}\begin{pmatrix} 0 & 0 & 1 \\ 0 & 0 & 0 \\ 1 & 0 & 0 \end{pmatrix}_{\ell,\ell'}, \tag{A3e}$$

$$\left(h^{(\mathrm{SOC})}_{\boldsymbol{k},\eta}\right)_{\rho,\ell,\boldsymbol{G};\rho',\ell',\boldsymbol{G}'} = \frac{\delta_{\boldsymbol{G},\boldsymbol{G}'}}{2}\begin{pmatrix} (h^{\mathrm{SOC},l=1}_\eta)_{\rho,\rho'} & 0 & (h^{\mathrm{SOC},l=1}_\eta)_{\rho,\rho'} \\ 0 & 0 & 0 \\ (h^{\mathrm{SOC},l=1}_\eta)_{\rho,\rho'} & 0 & (h^{\mathrm{SOC},l=1}_\eta)_{\rho,\rho'} \end{pmatrix}. \tag{A3f}$$

Here $\boldsymbol{\rho}_\theta = e^{i\theta\rho_3/2}\boldsymbol{\rho}e^{-i\theta\rho_3/2}$, and $\boldsymbol{q}_1$ connects the K and K' points in the MBZ; the tunneling matrices are

$$T_{\delta\boldsymbol{G}} = \sum_{j=-1,0,1} \delta_{\delta\boldsymbol{G}+\boldsymbol{A}_j,0}\left[w_0\rho_0 + w_1\begin{pmatrix} 0 & \omega^j \\ \omega^{-j} & 0 \end{pmatrix}\right],$$
$$\omega = e^{i\frac{2\pi}{3}}, \quad \boldsymbol{A}_0 = 0, \quad \boldsymbol{A}_1 = \boldsymbol{G}_1, \quad \boldsymbol{A}_2 = \boldsymbol{G}_1 + \boldsymbol{G}_2, \tag{A4}$$

with the property $T^\dagger_{\delta\boldsymbol{G}} = T_{\delta\boldsymbol{G}}$ and $\rho_x T_{\delta\boldsymbol{G}}\rho_x = T^*_{\delta\boldsymbol{G}}$; and the spin-orbit components are,

$$h^{\mathrm{SOC},l=1}_\eta = \lambda_\mathrm{I} s_z\eta + \lambda_\mathrm{R}\left(\eta\rho_x s_y - \rho_y s_x\right) + \lambda_\mathrm{KM}\eta\rho_z s_z + m\rho_z. \tag{A5}$$

This completes the continuum model in momentum space.

Appendix B: Pairing states in the opposite limit

In this appendix, we complement the discussion of Sec. III of the main text and present the details of the evolution of pairing states when first turning on λ_I, before λ_R, which is illustrated schematically in Fig. 2(b). This provides important insights into the form of the pairing state in the limit $\lambda_\mathrm{R} \ll \lambda_\mathrm{I}$.

As follows readily by inspection of Table I, the set of point symmetries (apart from time-reversal) for $\lambda_\mathrm{R} = 0$, $\lambda_\mathrm{I} \neq 0$ is generated by C_{3z}, $\mathrm{SO}(2)_s$, and $C_{2z}^{s'}$. Upon noting that the first of these symmetry operations commutes with the latter two, it is readily seen that they form the point group $C_3 \times D_\infty$, where D_∞ is generated by $\mathrm{SO}(2)_s$ and $C_{2z}^{s'}$ and, thus, can be thought of as D_n in the limit $n \to \infty$.

As in the main text, we start from the A_g^1 singlet and the B_u^3 triplet defined in Eq. (3.3) as the two parent pairing states in the limit without SOC, $\lambda_\mathrm{R} = \lambda_\mathrm{I} = 0$. Transforming trivially under C_{3z}, $\mathrm{SO}(2)_s$, and $C_{2z}^{s'}$, the A_g^1 singlet transitions into the pairing state of IR Σ_+^A of $C_3 \times D_\infty$ (here the superscript indicates the IR A of C_3 and Σ_+ labels the trivial IR D_∞); since $\mathrm{SO}(3)_s$ and C_{2z} are broken, an additional triplet component (from B_u^3) along the z direction is admixed and the order parameter can be written as

$$\psi_{\boldsymbol{k},\eta} = \chi_{\boldsymbol{k},\eta}, \qquad \boldsymbol{d}_{\boldsymbol{k},\eta} = \alpha_1 \eta \chi_{\boldsymbol{k},\eta} \boldsymbol{e}_z, \tag{B1}$$

where α_1 is proportional to λ_I for small λ_I. No triplet component in the xy-plane can be admixed due to $\mathrm{SO}(2)_s$. This includes the remaining two triplet components of B_u^3, which belong to the IR Π^A of $C_3 \times D_\infty$ (as above, the superscript A indicates the fact that the state transforms trivially under C_{3z} and Π is defined as the two-dimensional IR of D_∞ with components transforming as (x, y) under it). These symmetries do not allow for singlet-triplet admixture in this state and the two basis functions of the order parameter simply read as

$$\begin{pmatrix} \psi_{\boldsymbol{k},\eta}^1 \\ \psi_{\boldsymbol{k},\eta}^2 \end{pmatrix} = 0, \qquad \begin{pmatrix} \boldsymbol{d}_{\boldsymbol{k},\eta}^1 \\ \boldsymbol{d}_{\boldsymbol{k},\eta}^2 \end{pmatrix} = \eta \chi_{\boldsymbol{k},\eta} \begin{pmatrix} \boldsymbol{e}_x \\ \boldsymbol{e}_y \end{pmatrix}. \tag{B2}$$

If we eventually also turn on λ_R, we have to arrive at the same IRs and associated pairing states as discussed in Sec. III. However, as long as $\lambda_\mathrm{R} \ll \lambda_\mathrm{I}$, the relative strength of the different admixed components can differ. For the Σ_+^A state in Eq. (B1), breaking $\mathrm{SO}(2)_s$ and $C_{2z}^{s'}$ will add in-plane triplet components,

$$\psi_{\boldsymbol{k},\eta} = \chi_{\boldsymbol{k},\eta}, \qquad \boldsymbol{d}_{\boldsymbol{k},\eta} = \alpha_1 \eta \, \chi_{\boldsymbol{k},\eta} \boldsymbol{e}_z + \alpha_2 \begin{pmatrix} X_{\boldsymbol{k}} \\ Y_{\boldsymbol{k}} \\ 0 \end{pmatrix} + \alpha_3 \, \eta \begin{pmatrix} 2X_{\boldsymbol{k}} Y_{\boldsymbol{k}} \\ X_{\boldsymbol{k}}^2 - Y_{\boldsymbol{k}}^2 \\ 0 \end{pmatrix}. \tag{B3}$$

As required, it is of the same form as Eq. (3.8a) [or Eq. (3.8b) for that matter], but the relative weights are different since $\alpha_{2,3} \ll \alpha_1$ in Eq. (B3) for $\lambda_\mathrm{R} \ll \lambda_\mathrm{I}$ [as compared to $\alpha_{1,2} \gg \alpha_3$ in Eq. (3.8a) for $\lambda_\mathrm{I} \ll \lambda_\mathrm{R}$].

Finally, the Π^A state in Eq. (B2) becomes the E state of $\widetilde{C}_3$. Its order parameter is again of the form of Eq. (3.7), but with the crucial difference that, this time, all three coefficients $\alpha_{1,2,3}$ are small in λ_R.

Appendix C: Diode effect of the E state

In this appendix, we discuss the free energy expansion and associated critical current for pairing in the E representation, introduced in Sec. III of the main text.

1. Free energy

As opposed to Eq. (3.9), we here use the "chiral basis", $c_\pm = (c_1 \mp i c_2)/2$, as it will be more convenient. Generalizing to finite momentum pairing, $c_\pm \to c_\pm(\boldsymbol{q})$, the symmetries of the system act as

$$C_{3z}^s: \quad (c_+(\boldsymbol{q}), c_-(\boldsymbol{q})) \quad \longrightarrow \quad (\omega c_+(C_{3z}\boldsymbol{q}), \omega^* c_-(C_{3z}\boldsymbol{q})), \quad \omega = e^{i\frac{2\pi}{3}}, \tag{C1a}$$

$$\Theta_s: \quad (c_+(\boldsymbol{q}), c_-(\boldsymbol{q})) \quad \longrightarrow \quad (c_-^*(-\boldsymbol{q}), c_+^*(-\boldsymbol{q})). \tag{C1b}$$

Neglecting the momentum dependence of the quartic terms, b_1 and b_2, the free energy reads

$$\mathcal{F}[\{c_\pm(\boldsymbol{q})\}] \sim \sum_{\boldsymbol{q}} \left[a_{\boldsymbol{q}-2e\boldsymbol{A}} \left(|c_+(\boldsymbol{q})|^2 + |c_-(\boldsymbol{q})|^2 \right) + \delta a_{\boldsymbol{q}-2e\boldsymbol{A}} \left(|c_+(\boldsymbol{q})|^2 - |c_-(\boldsymbol{q})|^2 \right) + \left(\alpha_{\boldsymbol{q}-2e\boldsymbol{A}} c_+^*(\boldsymbol{q}) c_-(\boldsymbol{q}) + \text{c.c.} \right) \right]$$

$$+ \sum_{\boldsymbol{q}_1, \boldsymbol{q}_2, \boldsymbol{q}_3, \boldsymbol{q}_4} \delta_{\boldsymbol{q}_1 + \boldsymbol{q}_3, \boldsymbol{q}_2 + \boldsymbol{q}_4} \left[b_1 \left(\sum_{\mu=\pm} c_\mu^*(\boldsymbol{q}_1) c_\mu(\boldsymbol{q}_2) \right) \left(\sum_{\mu=\pm} c_\mu^*(\boldsymbol{q}_3) c_\mu(\boldsymbol{q}_4) \right) + b_2\, c_+^*(\boldsymbol{q}_1) c_+(\boldsymbol{q}_2) c_-^*(\boldsymbol{q}_3) c_-(\boldsymbol{q}_4) \right] \tag{C2}$$

where $a_{\boldsymbol{q}}, \delta a_{\boldsymbol{q}} \in \mathbb{R}$, $\alpha(\boldsymbol{q}) \in \mathbb{C}$ obeying

$$a_{\boldsymbol{q}} = a_{C_{3z}\boldsymbol{q}},\ \delta a_{\boldsymbol{q}} = \delta a_{C_{3z}\boldsymbol{q}},\ \alpha_{\boldsymbol{q}} = \omega^* \alpha_{C_{3z}\boldsymbol{q}} \quad \text{and} \quad a_{\boldsymbol{q}} = a_{-\boldsymbol{q}},\ \delta a_{\boldsymbol{q}} = -\delta a_{-\boldsymbol{q}},\ \alpha_{\boldsymbol{q}} = \alpha_{-\boldsymbol{q}} \tag{C3}$$

as follows from Eqs. (C1a) and (C1b), respectively. Consequently, both $\delta a_{\boldsymbol{q}}$ and $\alpha_{\boldsymbol{q}}$ have to vanish at $\boldsymbol{q} = 0$, reproducing the form of the free energy in [50]. Note that α will also have to vanish at finite $\boldsymbol{q}$, if we only have Ising SOC ($\lambda_{\text{R}} = 0$): in this case, the order parameter will be the Π^A state in Eq. (B2) [see also Fig. 2(b)] and the $\text{SO}(2)_s$ rotation symmetry in Table I prohibits finite $\alpha_{\boldsymbol{q}}$ in Eq. (C2).

To illustrate these statements and the microscopic origin of the terms in the free energy (C2), consider the following minimal low-energy, mean-field model for pairing in the E representation,

$$H^E = \sum_{\boldsymbol{k}, \eta, s, s'} f_{\boldsymbol{k}, \eta, s}^\dagger \left(h_{\boldsymbol{k}; \eta}^{\text{LE}} \right)_{s, s'} f_{\boldsymbol{k}, \eta, s'} + \sum_{\boldsymbol{k}, \boldsymbol{q}, s, s'} \left[f_{\boldsymbol{k}+\boldsymbol{q}, +, s}^\dagger \sum_{\mu=\pm} c_\mu(\boldsymbol{q}) \left(s^\mu \right)_{s, s'} f_{-\boldsymbol{k}, -, s'}^\dagger + \text{H.c.} \right] + \frac{1}{g_E} \sum_{\mu=\pm} |c_\mu(\boldsymbol{q})|^2, \tag{C4}$$

using the low-energy fermions $f_{\boldsymbol{k}, \eta, s}$ introduced in Sec. II C and $s^\pm = s_x \pm i s_y$. This is equivalent to setting $\alpha_j = 0$ and $\chi_{\boldsymbol{k}, \eta} = 1$ in Eq. (3.7). It is easy to check that applying the representations of the symmetries C_{3z}^s and Θ_s in Table I to the fermions in Eq. (C4) reproduces Eq. (C1). We parametrize the normal-state Hamiltonian in Eq. (C4) as

$$h_{\boldsymbol{k}; +}^{\text{LE}} = \epsilon_{\boldsymbol{k}} s_0 + \boldsymbol{g}_{\boldsymbol{k}} \cdot \boldsymbol{s}, \qquad h_{\boldsymbol{k}; -}^{\text{LE}} = s_y (h_{-\boldsymbol{k}; +}^{\text{LE}})^* s_y, \tag{C5}$$

i.e., explicitly restrict the analysis to time-reversal symmetric normal states. As such, any diode effect must come from the pairing-induced time-reversal-symmetry breaking. Unless further symmetries are imposed (if λ_{R} or λ_{I} vanishes), the only additional constraints on the normal-state Hamiltonian come from C_{3z} and read as

$$\epsilon_{\boldsymbol{k}} = \epsilon_{C_{3z}\boldsymbol{k}}, \qquad \boldsymbol{g}_{\boldsymbol{k}} = C_{3z} \boldsymbol{g}_{C_{3z}\boldsymbol{k}}. \tag{C6}$$

Integrating out the fermions in an action description of Eq. (C4) and expanding the resultant effective action in terms of c_μ, one can readily derive all prefactors in the free-energy expansion (C2). Defining the functional

$$\mathcal{I}[X(i\omega_n, \boldsymbol{k}, \boldsymbol{q})] := T \sum_{\omega_n} \frac{4}{N} \sum_{\boldsymbol{k} \in \text{MBZ}} \frac{X(i\omega_n, \boldsymbol{k}, \boldsymbol{q})}{\left[(i\omega_n - \epsilon_{\boldsymbol{k}+\boldsymbol{q}/2})^2 - \boldsymbol{g}_{\boldsymbol{k}+\boldsymbol{q}/2}^2 \right] \left[(i\omega_n + \epsilon_{\boldsymbol{k}-\boldsymbol{q}/2})^2 - \boldsymbol{g}_{\boldsymbol{k}-\boldsymbol{q}/2}^2 \right]}, \tag{C7}$$

where ω_n denote fermionic Matsubara frequencies, we have

$$a_{\boldsymbol{q}} = \frac{1}{g_E} + \mathcal{I}\left[(i\omega_n + \epsilon_{\boldsymbol{k}-\frac{\boldsymbol{q}}{2}})(i\omega_n - \epsilon_{\boldsymbol{k}+\frac{\boldsymbol{q}}{2}}) + g_{\boldsymbol{k}+\frac{\boldsymbol{q}}{2}}^z g_{\boldsymbol{k}-\frac{\boldsymbol{q}}{2}}^z \right], \tag{C8}$$

$$\delta a_{\boldsymbol{q}} = \mathcal{I}\left[i\omega_n (g_{\boldsymbol{k}+\frac{\boldsymbol{q}}{2}}^z + g_{\boldsymbol{k}-\frac{\boldsymbol{q}}{2}}^z) + g_{\boldsymbol{k}+\frac{\boldsymbol{q}}{2}}^z \epsilon_{\boldsymbol{k}+\frac{\boldsymbol{q}}{2}} - g_{\boldsymbol{k}-\frac{\boldsymbol{q}}{2}}^z \epsilon_{\boldsymbol{k}-\frac{\boldsymbol{q}}{2}} \right], \tag{C9}$$

$$\alpha_{\boldsymbol{q}} = -\mathcal{I}\left[(g_{\boldsymbol{k}+\frac{\boldsymbol{q}}{2}}^x - i g_{\boldsymbol{k}+\frac{\boldsymbol{q}}{2}}^y)(g_{\boldsymbol{k}-\frac{\boldsymbol{q}}{2}}^x - i g_{\boldsymbol{k}-\frac{\boldsymbol{q}}{2}}^y) \right]. \tag{C10}$$

While it is straightforward to evaluate all involved Matsubara sums, we can already see immediately, using Eq. (C6), that all properties in Eq. (C3) are obeyed—as required by symmetry. Furthermore, in accordance with Eq. (2.4), it holds $g^{x,y} = 0$ if we only have Ising SOC, $\lambda_{\text{R}} = 0$, leading to $\alpha_{\boldsymbol{q}} = 0$ in Eq. (C10); this, in turn, agrees with our statement above that the $\text{SO}(2)_s$ symmetry forces α to vanish in the free energy (C2).

2. Critical current

We next discuss the resulting critical current and diode effect. To simplify the presentation, let us first set $\alpha = 0$. As discussed in Sec. VA, the critical current is computed by setting $c_\mu(\boldsymbol{q}) = \Psi_\mu(\boldsymbol{q}_0)\delta_{\boldsymbol{q},\boldsymbol{q}_0}$, with $\Psi_\mu(\boldsymbol{q}_0)$ chosen to minimize $\mathcal{F}$ (at $\boldsymbol{A} = 0$), and studying the maximum value of

$$\boldsymbol{J}_{\boldsymbol{q}_0} = -\partial_{\boldsymbol{A}}\mathcal{F}[\{\Psi_\mu(\boldsymbol{q}_0)\delta_{\boldsymbol{q},\boldsymbol{q}_0}\}]|_{\boldsymbol{A}=0} = 2e\left[(|\Psi_+(\boldsymbol{q}_0)|^2 + |\Psi_-(\boldsymbol{q}_0)|^2)\partial_{\boldsymbol{q}_0}a_{\boldsymbol{q}_0} + (|\Psi_+(\boldsymbol{q}_0)|^2 - |\Psi_-(\boldsymbol{q}_0)|^2)\partial_{\boldsymbol{q}_0}\delta a_{\boldsymbol{q}_0}\right] \quad \text{(C11)}$$

along a given direction $\hat{n}$.

If $b_2 > 0$, which is the sign that one obtains within mean-field theory [53], and we use the *global minimum* of the free energy for $\Psi_\mu(\boldsymbol{q}_0)$, we will have $\Psi_{\text{sign}(\delta a_{\boldsymbol{q}_0})}(\boldsymbol{q}_0) = 0$ and $\Psi_{-\text{sign}(\delta a_{\boldsymbol{q}_0})}(\boldsymbol{q}_0) = \sqrt{(|\delta a_{\boldsymbol{q}_0}| - a_{\boldsymbol{q}_0})/(2b_1)}$. Inserting this into the expression for the current in Eq. (C11) yields

$$\boldsymbol{J}_{\boldsymbol{q}} = e(|\delta a_{\boldsymbol{q}}| - a_{\boldsymbol{q}})(\partial_{\boldsymbol{q}}a_{\boldsymbol{q}} - \text{sign}(\delta a_{\boldsymbol{q}})\partial_{\boldsymbol{q}}\delta a_{\boldsymbol{q}})/b_1. \quad \text{(C12)}$$

Recalling Eq. (C3), we see that it holds $\boldsymbol{J}_{\boldsymbol{q}} = -\boldsymbol{J}_{-\boldsymbol{q}}$, implying $J_c(\hat{n}) = J_c(-\hat{n})$ and, hence, ruling out a diode effect.

It can be shown by explicit calculation that this is also the case when finite α are taken into account (or when $b_2 < 0$). In fact, this can be understood more generally, without having to neglect the momentum dependence of higher-order terms in $\mathcal{F}$ or even without resorting to an expansion of the free energy—it is just a manifestation of the fact that the normal state above the superconducting phase has time-reversal symmetry. To see this formally in our current description, let us define

$$f(\psi_\mu, \boldsymbol{q}_0) := \mathcal{F}[\{c_\mu(\boldsymbol{q}) = \psi_\mu\delta_{\boldsymbol{q},\boldsymbol{q}_0}\}]. \quad \text{(C13)}$$

Time-reversal symmetry implies that the free-energy $\mathcal{F}$ is invariant under Eq. (C1b) which leads to the constraint

$$f(\psi_\mu, \boldsymbol{q}) = f(\psi_{-\mu}^*, -\boldsymbol{q}) \quad \text{(C14)}$$

on the function defined in Eq. (C13). Denoting the minimum of $f(\psi_\mu, \boldsymbol{q})$ at fixed $\boldsymbol{q}$ by $\Psi_\mu(\boldsymbol{q})$ (note that for generic $\boldsymbol{q}$ this is expected to be unique), Eq. (C14) then implies

$$\Psi_\mu(-\boldsymbol{q}) = \Psi_{-\mu}^*(\boldsymbol{q}). \quad \text{(C15)}$$

With this, we are in position to relate $\boldsymbol{J}_{\boldsymbol{q}} = 2e(\partial_{\boldsymbol{q}}f(\psi_\mu, \boldsymbol{q}))|_{\psi_\mu=\Psi_\mu(\boldsymbol{q})}$ and $\boldsymbol{J}_{-\boldsymbol{q}}$:

$$\boldsymbol{J}_{-\boldsymbol{q}} = 2e\left(\partial_{\boldsymbol{q}'}f(\psi_\mu, \boldsymbol{q}')\right)|_{\boldsymbol{q}'=-\boldsymbol{q};\,\psi_\mu=\Psi_\mu(-\boldsymbol{q})} \quad \text{(C16)}$$

$$= -2e\left(\partial_{\boldsymbol{q}'}f(\psi_\mu, -\boldsymbol{q}')\right)|_{\boldsymbol{q}'=\boldsymbol{q};\,\psi_\mu=\Psi_\mu(-\boldsymbol{q})} \quad \text{(C17)}$$

$$\overset{(C14)}{=} -2e\left(\partial_{\boldsymbol{q}'}f(\psi_{-\mu}^*, \boldsymbol{q}')\right)|_{\boldsymbol{q}'=\boldsymbol{q};\,\psi_\mu=\Psi_\mu(-\boldsymbol{q})} \quad \text{(C18)}$$

$$\overset{(C15)}{=} -2e\left(\partial_{\boldsymbol{q}'}f(\psi_\mu, \boldsymbol{q}')\right)|_{\boldsymbol{q}'=\boldsymbol{q};\,\psi_\mu=\Psi_\mu(\boldsymbol{q})} \quad \text{(C19)}$$

$$= -\boldsymbol{J}_{\boldsymbol{q}}. \quad \text{(C20)}$$

Form this immediately follows that there will be no diode effect.

However, as mentioned in Sec. IV D, the situation is different if the system remains in the *local minimum* of $\mathcal{F}$ which is smoothly connected to the configuration of the superconductor without external current. This is expected to be particularly relevant when the time-reversal-symmetry-breaking order parameter in Eq. (4.3) orders at temperatures well above the resistive superconducting transition.

As before, we illustrate this situation in the particularly simple case where $\alpha = 0$ in Eq. (C2). Let us assume that $b_1, b_2 > 0$, $a < 0$ and the superconductor, without current, has $c_+ \neq 0$, $c_- = 0$. Then the Ising-like order parameter in Eq. (4.3) is positive, $\mathcal{C} > 0$, and

$$\Psi_+(\boldsymbol{q}) = \sqrt{(|\delta a_{\boldsymbol{q}}| - a_{\boldsymbol{q}})/(2b_1)}, \quad \Psi_-(\boldsymbol{q}) = 0, \quad \text{as long as } \delta a_{\boldsymbol{q}} > \frac{a_{\boldsymbol{q}}b_2}{2b_1 + b_2} \quad \text{(C21)}$$

at the associated local minimum in the presence of a current-induced finite-momentum order parameter (if $\delta a_{\boldsymbol{q}}$ is smaller than the indicated lower bound, the minimum becomes locally unstable). We see that, irrespective of the direction of $\boldsymbol{q}$, the Ising-like order parameter $\mathcal{C}$ now varies smoothly and remains positive when turning on $\boldsymbol{q}$. Assuming

that the inequality in Eq. (C21) is valid for all $\boldsymbol{q}$ relevant to determine the critical current, we can determine the latter by inserting this into Eq. (C12), yielding

$$\boldsymbol{J_q} = e(|\delta a_{\boldsymbol{q}}| - a_{\boldsymbol{q}})(\partial_{\boldsymbol{q}} a_{\boldsymbol{q}} + \partial_{\boldsymbol{q}} \delta a_{\boldsymbol{q}})/b_1. \tag{C22}$$

Since $\delta a_{\boldsymbol{q}}$ is an odd function of $\boldsymbol{q}$, see Eq. (C3), we generally have $\boldsymbol{J_q} \neq -\boldsymbol{J_{-q}}$ and a diode effect becomes possible.

Note that this is different for the nematic state: if $b_2 < 0$, we obtain a nematic superconducting state, which—in analogy to the time-reversal-odd composite order parameter in Eq. (4.3)—can be characterized by the nematic composite order parameter

$$\mathcal{N}_j^E := \sum_{\boldsymbol{q}} \begin{pmatrix} \mathrm{Re}\left[c_+^*(\boldsymbol{q}) c_-(\boldsymbol{q}) \right] \\ \mathrm{Im}\left[c_+^*(\boldsymbol{q}) c_-(\boldsymbol{q}) \right] \end{pmatrix}_j. \tag{C23}$$

Note that $c_+^* c_- = \mathcal{N}_1^E + i\mathcal{N}_2^E \to \omega c_+^* c_-$ under C_{3z} while remaining invariant under Θ_s. Breaking a discrete symmetry, $\mathcal{N}_j^E$ can order at a non-zero temperature T^*. Just as in case of the chiral state, let us assume that T^* is significantly larger than the resistive superconducting transition and that, when applying a current, the superconducting order parameter adiabatically follows the *local minimum* that has already been chosen spontaneously at T^* (note that sixth order terms need to be added to Eq. (C2) to break the artificial continuous rotational symmetry of the quartic free-energy expansion without current, see [50]). Writing as before $c_\mu(\boldsymbol{q}) = \Psi_\mu(\boldsymbol{q}_0)\delta_{\boldsymbol{q},\boldsymbol{q}_0}$, it holds under these assumptions

$$\phi(\boldsymbol{q}) = \phi(-\boldsymbol{q}), \quad |\Psi_+(\boldsymbol{q})| = |\Psi_-(-\boldsymbol{q})|, \tag{C24}$$

where ϕ is defined via $\Psi_+^*(\boldsymbol{q})\Psi_-(\boldsymbol{q}) = |\Psi_+^*(\boldsymbol{q})||\Psi_-(\boldsymbol{q})|e^{i\phi(\boldsymbol{q})}$. It is a smooth function of momentum such that $\mathcal{N}_j^E$ varies smoothly when applying a current. The properties in Eq. (C24) follow from $a_{\boldsymbol{q}} = a_{-\boldsymbol{q}}$, $\delta a_{\boldsymbol{q}} = -\delta a_{-\boldsymbol{q}}$, $\alpha_{\boldsymbol{q}} = \alpha_{-\boldsymbol{q}}$ in Eq. (C3) and that $|\Psi_+(\boldsymbol{q}=0)| = |\Psi_-(\boldsymbol{q}=0)|$. From this we get

$$\boldsymbol{J_q} = 2e\left[\partial_{\boldsymbol{q}} a_{\boldsymbol{q}} \sum_\mu |\Psi_\mu(\boldsymbol{q})|^2 + \partial_{\boldsymbol{q}} \delta a_{\boldsymbol{q}} \sum_\mu \mu |\Psi_\mu(\boldsymbol{q})|^2 + 2|\Psi_+(\boldsymbol{q})||\Psi_-(\boldsymbol{q})|\mathrm{Re}\left(\partial_{\boldsymbol{q}} \alpha_{\boldsymbol{q}} e^{i\phi(\boldsymbol{q})} \right) \right]. \tag{C25}$$

We, thus, see that $\boldsymbol{J_q} = -\boldsymbol{J_{-q}}$ and no diode effect is possible as expected since neither the normal nor the superconducting state breaks time-reversal symmetry (in the absence of an applied current).

Appendix D: Patch theory expansion

To obtain analytic expressions from (5.11), we consider $T \sim T_c$, with $T_c \sim v\Lambda_x e^{-1/(\nu g)}$ set by the energy cut-off of the patch, which is approximately set by the energy cut-off in the direction perpendicular to the patched Fermi surface, i.e. k_x direction. Assuming large density of states times the Cooper channel interaction strength, νg, we arrive at $T \sim v\Lambda_x$. With this we may expand the hyperbolic tangents in the kernel of $\Gamma(\boldsymbol{q})$, $\tanh(x) \simeq x - x^3/3 + 2x^5/15 + O(x^7)$, i.e.

$$\Gamma^p(\boldsymbol{q}) \simeq \int_{-\Lambda_y}^{\Lambda_y} \frac{\mathrm{d}k_y}{2\pi} \int_{-\Lambda_x}^{\Lambda_x} \frac{\mathrm{d}\delta k_x}{4\pi} \frac{1}{\xi_1 + \xi_2} \left[\frac{\xi_1}{2T} + \frac{\xi_2}{2T} - \frac{1}{3}\left(\frac{\xi_1}{2T}\right)^3 - \frac{1}{3}\left(\frac{\xi_2}{2T}\right)^3 + \frac{2}{15}\left(\frac{\xi_1}{2T}\right)^5 + \frac{2}{15}\left(\frac{\xi_2}{2T}\right)^5 \right],$$
$$\xi_1 = v(\delta k_x + \delta q_x/2) - \alpha_+(k_y + q_y/2)^2,$$
$$\xi_2 = v(\delta k_x - \delta q_x/2) - \alpha_-(k_y - q_y/2)^2. \tag{D1}$$

Based on the above reasoning, $\xi_i/(2T) \lesssim 1/2$, therefore justifying the order of the expansion. The expression (D1) affords an analytic integration; performing such integration and extracting the leading coefficients, as per the expansion given in Eq. (5.13), gives

$$a_1 = \frac{(\alpha_+ - \alpha_-)\, v\Lambda_x \Lambda_y^3 \left(-126T^2 + 14v^2\Lambda_x^2 + 9\left(\alpha_-^2 + \alpha_+^2\right)\Lambda_y^4\right)}{3024T^5}, \tag{D2}$$

$$a_2 = \frac{v^2 \Lambda_x \Lambda_y \left(45T^2 - 5v^2\Lambda_x^2 - 3\left(\alpha_+^2 - \alpha_-\alpha_+ + \alpha_-^2\right)\Lambda_y^4\right)}{360T^5(8\pi^2)}, \tag{D3}$$

$$a_3 = \frac{(\alpha_+ - \alpha_-)\, v^3 \Lambda_x \Lambda_y^3}{144T^5(8\pi^2)},$$

$$a_4 = -\frac{v^4 \Lambda_x \Lambda_y}{192 T^5 (8\pi^2)},$$

$$c = \frac{\Lambda_x \Lambda_y^3 \left(105 \left(3\alpha_+^2 + \alpha_- \alpha_+ + 3\alpha_-^2\right) T^2 - 7 \left(6\alpha_+^2 + \alpha_- \alpha_+ + 6\alpha_-^2\right) v^2 \Lambda_x^2 + 9 \left(-7\alpha_1^4 + \alpha_- \alpha_+^3 + \alpha_-^2 \alpha_+^2 + \alpha_-^3 \alpha_1 - 7\alpha_-^4\right) \Lambda_y^4\right)}{3780 T^5 (8\pi^2)}.$$

In particular, we see that a_1 and a_2 vanish as $\alpha_+ - \alpha_- \to 0$, which we stated and used in Sec. V B. We emphasize that this also holds when no additional approximations are made in the evaluation of Eq. (5.11). Since Γ in Eq. (5.11) is invariant under $\delta q_x \to -\delta q_x$ and simultaneous exchange $\alpha_+ \leftrightarrow \alpha_-$, we immediately conclude that

$$a_{1,3}(\alpha_+, \alpha_-) = -a_{1,3}(\alpha_-, \alpha_+), \qquad a_{2,4}(\alpha_+, \alpha_-) = a_{2,4}(\alpha_-, \alpha_+) \tag{D4}$$

and, hence, $a_{1,3}(\alpha, \alpha) = 0$.

Appendix E: LG theory in the presence of strong spin-orbit coupling or intravalley pairing

1. Strong spin-orbit coupling

We look now at strong SOC, such that bands are non-degenerate. Explicitly, we work with the low energy bands that cross the Fermi level in the vicinity of $\boldsymbol{k}$; the band energies in valley η are denoted by $\xi_{\boldsymbol{k},\eta}$. These states are obtain by diagonalising the full tTLG noninteracting Hamiltonian (2.1b), in the presence of either valley polarization or applied magnetic field, which are captured by adding the perturbations

$$\delta h_1 = V_z \eta_z, \quad \delta h_2 = \boldsymbol{B} \cdot \boldsymbol{s} \tag{E1}$$

to h. In the absence of these perturbations, time-reversal symmetry is preserved, and the band energies satisfy $\xi_{\boldsymbol{k},+} = \xi_{-\boldsymbol{k},-}$.

To describe pairing between states at opposite valleys, we consider the effective interacting Hamiltonian

$$H = \sum_{\boldsymbol{k},\eta} \tilde{f}_{\boldsymbol{k},\eta}^\dagger \xi_{\boldsymbol{k},\eta} \tilde{f}_{\boldsymbol{k},\eta} - \frac{\tilde{g}}{2} \sum_{\boldsymbol{k},\boldsymbol{k}',\boldsymbol{q}} \tilde{f}_{\boldsymbol{k}+\boldsymbol{q},\eta}^\dagger \tilde{f}_{\boldsymbol{k}'-\boldsymbol{q},\eta'}^\dagger \tilde{f}_{\boldsymbol{k}',\eta'} \tilde{f}_{\boldsymbol{k},\eta},$$

where $\tilde{f}_{\boldsymbol{k},\eta}$ and $\tilde{f}_{\boldsymbol{k},\eta}^\dagger$ are annihilation and creation operators of electrons of valley η, in the low-energy bands crossing the Fermi level in the vicinity of $\boldsymbol{k}$. Due to strong SOC, this Hamiltonian is effectively spinless. It is important to keep in mind that, as a consequence of the underlying SOC, the electronic states created by $\tilde{f}_{\boldsymbol{k},\eta}^\dagger$ exhibit a momentum-dependent spin quantum number.

Performing a mean-field decoupling in the intervalley channel, we obtain

$$H = \sum_{\boldsymbol{k},\eta} \tilde{f}_{\boldsymbol{k},\eta}^\dagger \xi_{\boldsymbol{k},\eta} \tilde{f}_{\boldsymbol{k},\eta} + \frac{1}{2\tilde{g}} \sum_{\boldsymbol{q}} \Delta_{\boldsymbol{q}}^\dagger \Delta_{\boldsymbol{q}} + \frac{1}{2} \sum_{\boldsymbol{k},\boldsymbol{q}} \left[\tilde{f}_{\boldsymbol{k}+\boldsymbol{q},+}^\dagger \Delta_{\boldsymbol{q}} \tilde{f}_{-\boldsymbol{k},-}^\dagger + \text{H.c.}\right] \tag{E2}$$

where the complex scalar $\Delta_{\boldsymbol{q}}$ is the superconducting order parameter. As a result of the aforementioned momentum-dependent spin quantum number of the low-energy fermions, this single complex number describes a, in general, singlet-triplet mixed state; for $\boldsymbol{q} = 0$ pairing, the structure of the order parameter in terms of the physical spin basis is discussed in Sec. III of the main text. The associated Ginzburg-Landau expansion is analogous to the expression presented in the main text (5.4),

$$\mathcal{F} \sim \frac{1}{2} \sum_{\boldsymbol{q}} a_{\boldsymbol{q}} \Delta_{\boldsymbol{q}}^\dagger \Delta_{\boldsymbol{q}} + \mathcal{O}(\Delta^4), \quad a_{\boldsymbol{q}} = \frac{1}{\tilde{g}} - \Gamma(\boldsymbol{q}),$$

$$\Gamma(\boldsymbol{q}) = \frac{1}{2N} \sum_{\boldsymbol{k} \in \text{MBZ}} \frac{\tanh\left(\frac{\xi_{\boldsymbol{k}+\frac{\boldsymbol{q}}{2},+}}{2T}\right) + \tanh\left(\frac{\xi_{-\boldsymbol{k}+\frac{\boldsymbol{q}}{2},-}}{2T}\right)}{\xi_{\boldsymbol{k}+\frac{\boldsymbol{q}}{2},+} + \xi_{-\boldsymbol{k}+\frac{\boldsymbol{q}}{2},-}}. \tag{E3}$$

From which the expression for the current follows via Eq. (5.7).

2. Intravalley pairing

Finally, we state, without derivation, that for the case of intravalley, spin-singlet pairing with spin-degenerate bands—considered in the context of the toy-models of Sec. V C—the corresponding expression for $\Gamma(\boldsymbol{q})$ is

$$\Gamma(\boldsymbol{q}) = \frac{1}{2N} \sum_{\boldsymbol{k} \in \text{MBZ}} \frac{\tanh\left(\frac{\xi_{\boldsymbol{k}+\frac{\boldsymbol{q}}{2},+,\uparrow}}{2T}\right) + \tanh\left(\frac{\xi_{-\boldsymbol{k}+\frac{\boldsymbol{q}}{2},+,\downarrow}}{2T}\right)}{\xi_{\boldsymbol{k}+\frac{\boldsymbol{q}}{2},+,\uparrow} + \xi_{-\boldsymbol{k}+\frac{\boldsymbol{q}}{2},+,\downarrow}}. \tag{E4}$$